Field-Resolved Spectroscopy in the Gas Phase

Feldaufgelöste Spektroskopie in der Gasphase

Lukas Michael Fürst

Munich 2021

Field-Resolved Spectroscopy in the Gas Phase

Master Thesis
Faculty of Physics
Ludwig-Maximilians-University

Max Planck Institute of Quantum Optics
ATTOWORLD
Field-Resolved Infrared Metrology

submitted by
Lukas Michael Fürst
from Rosenheim

Munich
June 16, 2021

Supervisors: Priv. Doz. Dr. Ioachim Pupeza, Prof. Dr. Ferenc Krausz

Contents

Glossary

CEO carrier-envelope offset.

DFG difference frequency generation.

EC enhancement cavity.

EOM electro-optic modulator.

EOS electro-optic sampling.

FRS field-resolved spectroscopy.

FTIR Fourier-transform infrared.

FWHM full-width-at-half-maximum.

HITRAN high-resolution transmission molecular absorption.

IC input coupler.

IPDFG intra-pulse difference frequency generation.

LOD limit of detection.

MCT mercury-cadmium-telluride.

MIR mid-infrared.

NIR near-infrared.

PCF photonic crystal fiber.

ppb parts per billion.

ppm parts per million.

ppt parts per trillion.

SFG sum frequency generation.

SNR signal-to-noise ratio.

Abstract

Mid-infrared spectroscopy is a multifaceted approach to investigate the vibrational and rotational modes of molecules. Analyzing gas-phase samples in conjunction with novel technologies with high spectral resolution, especially frequency combs, enables high specificity. This is possible due to the longer coherence time of the resonant emission of gases compared to liquids. However, in the mid-infrared range, time-integrating frequency-domain spectroscopy suffers from limitations related to the dynamic range and noise figures of the detectors. In our group, it was recently demonstrated that field-resolved spectroscopy (FRS) analyzing the coherently emitted field by molecules excited by a few-cycle infrared pulse strongly mitigates these limitations, enabling a new sensitivity regime for liquid-phase samples.

In the present work, we explored the sensitivity potential of FRS for gas-phase ensembles, employing our octave-spanning (19.6-41.1 THz at the -30-dB-level), ultrafast mid-infrared source. Exploiting the time-resolving ability of electro-optic sampling, we measured the electric field of the molecular response in the background-free wake of the excitation, which increases the sensitivity compared to time-integrating spectroscopy. To push the sensitivity limit further, we increased the effective interaction length with the sample by employing an octave-spanning, mid-infrared enhancement cavity using reflective input coupling. Furthermore, we benchmarked the sensitivity of state-of-the-art time-integrating spectroscopy using an FTIR spectrometer and gaseous samples.

For FRS, we found a limit of detection of 1.9 ppb for methanol samples for an averaging time of 83 s and a sample cell length of 45 cm. We demonstrated an unprecedented retrievable concentration dynamic range of more than seven orders of magnitude. Improving this sensitivity by increasing interaction length with a multi pass cell by another two orders of magnitude seems feasible.

For comparison, we benchmarked a commercially available Fourier-transform infrared spectrometer and achieved a limit of detection of 818 ppb with a retrievable concentration dynamic range of 6.1×10^4 for an averaging time of 60 s and a sample cell length of 14 cm. We demonstrate the broad spectral coverage of our laser source using sample mixtures consisting of acetylene, methanol, and methane. Thereby, we achieved detection limits of 1.5 ppb (acetylene), 1.7 ppb (methanol) and 81 ppb (methane). Increasing the averaging time results in a detection limit of 913 ppt for methanol, but further averaging reveals negative effects of drifts in the detection setup setting in after typically 300 s.

The time-domain evolution of the methanol emission uncovers that the three branches are dominant at different time delays after the ultra-short pulse excitation. This was used to explain the spectra obtained with the enhancement cavity, which we built to increase the sensitivity. To this end, the peak sensitivity enhancement at 31 THz was determined to be 11 with a wavelength dependent amplitude ratio greater than 5 at 18.5 THz and 37.5 THz, spanning more than one octave.

To conclude, we have demonstrated a limit of detection, which is unique for this broad spectral coverage. In the future, the combination of FRS together with frequency comb techniques promises unprecedented specificity and sensitivity for gas-phase spectroscopy.

1 Introduction

Linear infrared spectroscopy is a powerful technique for exploring the vibrational and rotational modes of molecules [1]. It enables the investigation of a variety of samples ranging from proteins to trace gases, thus offering versatile fields of application [1][2][3]. The oscillatory modes are bond specific and therefore provide information about the molecular composition of the sample [4][5]. The current state-of-the-art tool for broadband mid-infrared spectroscopy is the Fourier-transform infrared (FTIR) spectrometer based on thermal sources, which enables measurements in the molecular fingerprint region (15-150 THz frequency) [4][6]. It is relatively cheap, compact, and necessitates small amounts of sample material [5]. There are widespread applications in industry, atmospheric science, or biomedicine [7].

A rapidly growing research area addresses the utilization of infrared spectroscopy in clinical applications, e.g., breath analysis for potential disease monitoring or disease detection using biofluids or breath [8][9]. Investigation of biological tissue, e.g., for cancer detection, requires detailed knowledge of the stability of infrared molecular fingerprints of individuals [5][10]. Detection of low-abundant components of blood can potentially enable earlier disease detection [9]. Therefore, the spectroscopic techniques need high sensitivity, but to probe multiple molecular types in parallel a broad spectral coverage must be sustained [10]. FTIR spectrometers based on thermal sources provide a broad spectral bandwidth, however, in the mid-infrared range, time-integrating frequency-domain spectroscopy suffers from limitations related to the dynamic range and noise figures of the detectors. In our group, it was recently demonstrated that field-resolved spectroscopy (FRS) mitigates these limitations, enabling a new sensitivity regime for liquid-phase samples [4].

Analyzing gas-phase samples in conjunction with novel technologies with high spectral resolution, especially frequency combs, enable high specificity due to the long coherence time of the bond-specific coherent emission [11]. This specificity advantage is less pronounced for liquid biomedical probes, but methods allowing for their

transfer to the gas phase can be applied [12].
Field-resolved detection can be achieved by electro-optic sampling (EOS). For EOS, a strong near-infrared (NIR) gate pulse is spatially and temporally overlapped with the mid-infrared (MIR) sample pulse and focused into a nonlinear crystal. The resulting NIR signal is measured by an ellipsometry setup and provides amplitude and phase information of the sample field [13]. Exploiting the time-resolving ability of EOS, we measure the electric field of this molecular response in the background-free wake of a few-cycle excitation pulse. Due to this separation, the molecular response of excitation powers that would saturate the detector are still detectable [14].

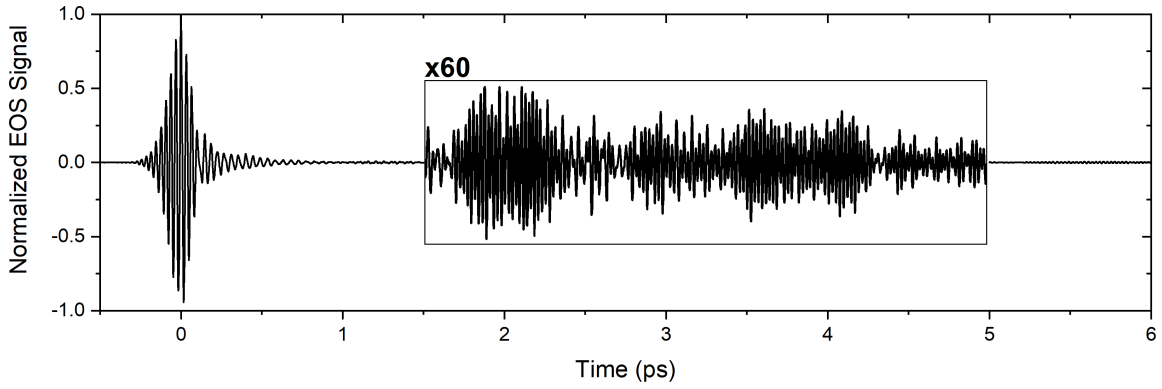

Figure 1.1: EOS trace for FRS. The main pulse excites molecular vibrations, which re-emit light causing a molecular multi-oscillator beating signal in the background-free wake of the excitation pulse (see inset). The free induction decay of gas-phase molecules extends over several picoseconds due to the longer coherence time of the resonant emission as compared to condensed-phase samples [11][15].

Figure 1.1 shows an exemplary sample trace measured using EOS. The time-domain signal of the molecular response can be explained by the free induction decay after an impulsive excitation by the few-cycle pulse. The main pulse at zero delay excites molecular oscillations in the sample, which re-emit light at characteristic frequencies causing multi-oscillator beating signals in the wake of the excitation. Analyzing the coherently emitted field by molecules, separated from the strong excitation with high intensity noise, grants higher sensitivity and detectable concentration dynamic range [4]. The sensitivity can be increased further by enhancing the molecular signal via longer interaction with the sample. Possible approaches are multi-pass cells and en-

hancement cavities (ECs) [16][17].
The goal of this thesis is to demonstrate a new sensitivity and detectable concentration dynamic range regime by FRS for gas-phase samples combined with broad spectral coverage. In the future, the combination of FRS together with frequency comb techniques promises unprecedented specificity and sensitivity in the gas phase [11].

Outline of this Thesis

We present a quantitative comparison between an FTIR spectrometer and FRS in the gas phase and investigate approaches for path-length-enhancement.
Chapter 2 encompasses the theoretical background of rotational-vibrational spectroscopy as well as linear infrared spectroscopy, e.g., FTIR spectroscopy and FRS. Furthermore, a short introduction on ECs is given.
The experimental work is described in **Chapter 3**. Two sample preparation protocols are presented to investigate the performance of the spectroscopic methods experimentally in the gas phase. The reproducibility of the sample handling and the tightness of the gas cell are verified and the parameters of the optical setups for the FTIR spectrometer and FRS is presented. To increase the effective interaction length with the sample and push the sensitivity limit further, we exhibit our octave-spanning, mid-infrared EC setup with reflective input coupling using a diamond wedge.
Chapter 4 comprises the experimental results. For quantitative comparison of state-of-the-art spectroscopy and FRS, we perform benchmark measurements using an FTIR spectrometer considering the sensitivity and detectable concentration dynamic range of gas-phase samples. Then, we explore the sensitivity potential of FRS, employing our octave-spanning (19.6-41.1 THz at the -30-dB-level), ultrafast mid-infrared source and characterize its performance for gas mixtures [18]. We determine the detection limits of FRS for different averaging times to identify the potential in terms of sensitivity. Moreover, the time-domain evolution of the methanol signal is investigated, which is necessary to explain the results obtained with the EC. To this end, the peak enhancement is quantified experimentally using a methanol test sample and the supported spectral bandwidth is characterized.
Chapter 5 concludes the thesis and provides an outlook for future experiments.

2 Theoretical Background

This section presents the theory behind gas-phase absorption spectra. The focus is on infrared spectra resulting from vibrational and rotational levels within the same electronic energy state. Moreover, the concept of linear infrared spectroscopy and two methods to retrieve the complex sample response are presented, i.e., Fourier-transform infrared spectroscopy and field-resolved spectroscopy. Finally, an approach for path length enhancement using a passive optical resonator is introduced.

2.1 Rotational-Vibrational Spectroscopy

In contrast to atoms, molecules have internal degrees of freedom, namely those of rotational and vibrational motion. The characteristic rotational and vibrational frequencies are determined by the transition frequencies between energy levels of a single molecule. Light stimulates these oscillations if its frequency corresponds to the transition frequency. All these oscillations together form the rotational-vibrational spectrum of absorption/emission lines. Thus, sample-characteristic information about chemical bonds can be gathered optically [19]. The absorption spectrum is most conveniently investigated in the gas phase. In the condensed phase, high inter-molecular interaction results in line broadening preventing the resolution of the rotational absorption lines.

In general, the internal degrees of freedom for molecules include vibration and rotation of all constituting atoms. When neglecting rotations, the simplest case of a diatomic molecule can be approximated by a harmonic oscillator with the well-known energy level separation [19]:

$$E_{vib,\nu} = \hbar\omega(\nu + \frac{1}{2}) \tag{2.1}$$

where $\hbar$ is the Planck constant divided by 2π and ν is the vibrational quantum number. Here, ω denotes the eigenfrequency of the harmonic oscillator, which corresponds to the transition frequency between subsequent energy levels.
A more realistic description is given by an anharmonic oscillator, which is characterized by an asymmetric potential curve (also called Born-Oppenheimer potential). This asymmetry emerges if the atomic distance is not comparable to the equilibrium position. Reasons for the asymmetry are short-ranged repulsive terms preventing the penetration of atoms or the dissipation of the molecules for large atomic distances. An asymmetric potential results in non-equidistant energy levels. In general, these levels are populated according to a Boltzmann distribution. At room temperature, population of excited vibrational states is usually negligible and only excitation from the vibrational ground state is to be considered [19].
Besides the oscillation of the inter-atomic distance, the molecule can rotate around different axes, with quantized energy. Therefore, rotational energy states are added to the level scheme, labeled with quantum number J. As the rotation period is typically much smaller than the vibration cycle, each vibrational level is extended by a fine structure of rotational states. Therefore, each purely vibrational transition is accompanied by absorption lines resulting from transitions of a vibrational and rotational level [19]. This results in an absorption spectrum plotted in Figure 2.1 for the example of methanol. The absorption frequencies are defined by the energy difference between the final and initial rotational-vibrational state.
Three different branches constitute the structure of a rotational-vibrational band: The central absorption peak is called the Q-branch. The frequency of the Q-branch is the fundamental eigenfrequency of the vibrational mode without any change in rotation quantum number (ΔJ=0). On the lower frequency side of the Q-branch the rotational lines form the so-called P-branch. These lines originate from transitions where the rotational quantum number J is reduced by one, resulting in $\Delta\nu$=+1 and ΔJ=$-$1. On the high-frequency side, the absorption lines are combined to the R-branch with $\Delta\nu$=+1 and ΔJ=+1. The strength of all absorption lines is defined by the population of the relevant initial state given by the Boltzmann distribution (illustrated by the line transparency in Figure 2.1) and the degeneracy of the energy levels.

Within the P and R-branch, the rotational lines are not evenly spaced. Asymmetric line spacing is caused by the anharmonic potential and coupling between rotation and vibration, resulting from interaction between the atoms inside a molecule. The

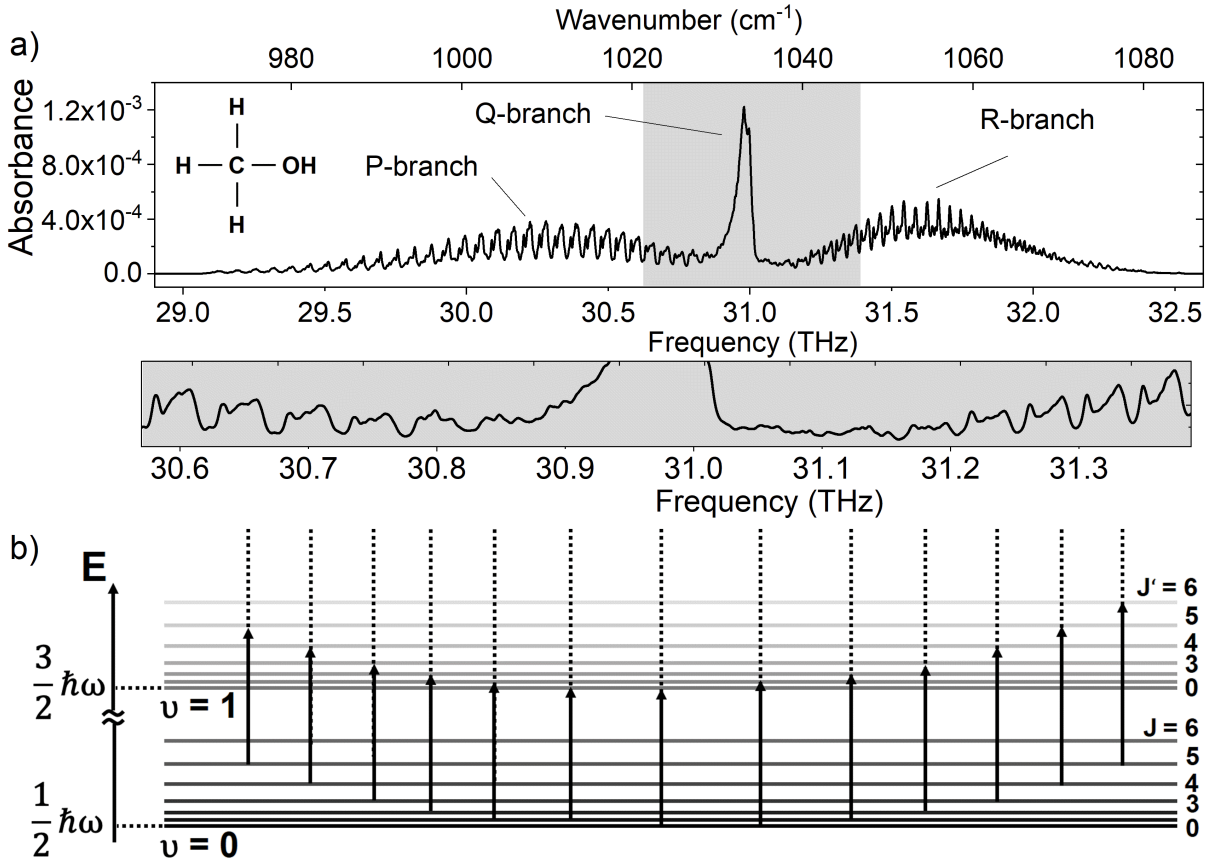

Figure 2.1: a) Simulated methanol absorption spectrum for 1 ppm concentration. b) Energy levels of rotational-vibrational states with line transparency indicating the population of each level. The Q-branch at f=31 THz emerges from the C-O stretch vibrational mode [20]. The P- and R-branch arise from transitions with a change in rotational quantum number J. The spacing of the rotational lines is not equidistant and the Q-branch is made up of several lines lying closely together.

coupling results in energy terms dependent on both quantum numbers making the lines non-evenly spaced, which also affects the Q-branch. In the harmonic case, the Q-branch is one single line. However, with different rotational line spacing the Q-branch is made up of multiple lines lying very close to the fundamental vibrational frequency. In the energy level picture these arise as the energy difference between levels with ΔJ=0 is not equal anymore [19]. In the time domain, when excited with an ultrashort pulse, the fact that the P and R-branch lines have different spacings cause beating features at different time delays (see Chapter 4).

Additionally, the rotational lines possess a substructure. This substructure originates from the lifted degeneracy of the rotational levels. In the case of methanol, the three principle axes of inertia are not equal, which introduces additional quantum numbers for the energy. These quantum numbers cause a splitting of the rotational lines for each rotational quantum number J [19].
In general, the appearance of infrared spectral bands depends on the symmetry of the molecule, which defines the molecule-specific selection rules. A transition is *infrared active* if a periodic change of a dipole moment is possible. For example, only certain carbon dioxide modes are infrared active and all nitrogen modes are infrared inactive. For some infrared-active modes, the transitions with ΔJ=0 are forbidden. Then, only the P and R-branch are visible in the absorption spectrum. An example is the fundamental mode of CO [19]. In the case of methanol, the Q-branch is allowed by the selection rules (see Figure 2.1).

2.2 Linear Infrared Spectroscopy

Infrared spectroscopy is a well-established and powerful technique for the investigation of a variety of samples ranging from proteins to trace gases, thus serving various fields of application [1][2][3]. The general scheme for infrared spectroscopy is shown in Figure 2.2. Infrared light interacts with a sample and the transmitted light is analyzed in terms of the different spectral components. Using this scheme, information about the molecular composition of the sample can be obtained.

The investigation of complex molecular samples, e.g., in biomedical applications,

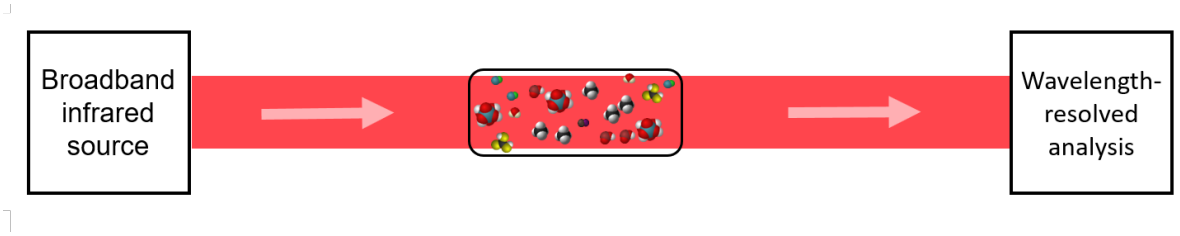

Figure 2.2: Illustration of linear infrared spectroscopy. A broadband light source illuminates a sample and the transmitted light is analyzed wavelength-resolved. Using this scheme, information about the molecular composition of the sample can be deducted from the complex sample response function.

requires a broadband light source, because different molecular species have different

spectral features, over several octaves in the MIR [1][4][2]. The relevant frequency region depends on the sample investigated.
In order to identify and quantify the sample constituents, we have to determine the response of the molecular sample to the incident light. For a linear interaction, the electric field after traversing the sample $\widetilde{E}_S(\omega)$ results from multiplication of the macroscopic complex sample response function $\widetilde{H}(\omega)$ by the incident electric field $\widetilde{E}_R(\omega)$ in the frequency domain.

$$\widetilde{E}_S(\omega) = \widetilde{H}(\omega) \cdot \widetilde{E}_R(\omega) \tag{2.2}$$

The complex response function contains the amplitude and phase information of the sample. Two common ways to determine this response function are described in the following section.

2.2.1 Fourier-Transform Infrared Spectroscopy

FTIR spectrometers are widely used devices and sometimes even interchanged with infrared spectroscopy [3]. They are by now highly engineered, optimized and commercially available. In the following paragraph, the basic theory behind the FTIR spectrometer is introduced and its advantages as well as disadvantages are discussed.
In an FTIR spectrometer, the wavelength-resolved analysis (see Figure 2.2) is realized using an interferometer. We will consider a Michelson interferometer (see Figure 2.3). Here, a beam splitter splits the input MIR light into two arms. Then, each beam undergoes path-dependent phase and amplitude changes. Afterwards, the beams are recombined and interfere depending on their mutual phase. In the simple example of equal optical path lengths, they interfere constructively at the detector [21]. The delay τ changes the group delay, i.e., the linear spectral phase, and thus the interference signal at the detector is modified. If we then scan over different delays, an intensity interferogram is recorded directly in the MIR. This can be achieved using an MCT detector, which suffer from bad noise figures. As the linear phase shift caused by the group delay is wavelength-dependent, the incident spectrum is obtained as the Fourier-transform of the intensity interferogram.
We will examine the case of a non-dispersive, i.e., symmetric setup, where the sample is placed after the interferometer (see Figure 2.3). From this FTIR spectrometer geometry, the sample response function is determined as follows: For slow detectors,

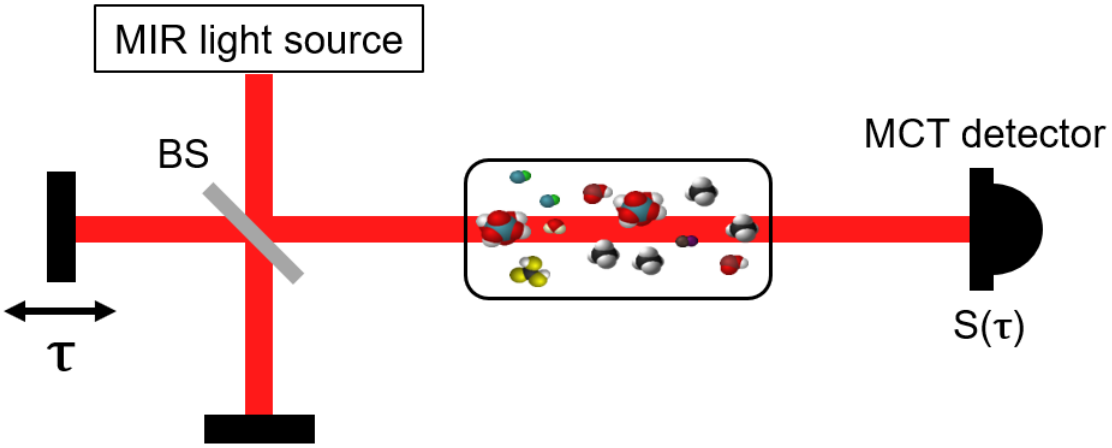

Figure 2.3: Symmetric Fourier-transform infrared spectrometer using a Michelson interferometer. Usually a thermal source sends MIR light to the interferometer. One interferometer arm is temporally delayed changing the interference at the output. While scanning over different delays, a mercury-cadmium-telluride (MCT) detector measures the intensity interferogram. The spectral information results from a Fourier transformation of the interferogram. In the case of a symmetric FTIR spectrometer the sample cell is placed before or after the interferometer.

the measured signal with an impinging electric field $E_{R/S}(t)$ for a reference (R) and sample (S) measurement, respectively, is written as the time integral:

$$S \propto \int_{\Delta T} E_{R/S}^2(t)\mathrm{d}t \tag{2.3}$$

with the measurement time per delay point, ΔT. The reference scan refers to the sample container being empty. Then, the measured intensity from the input field $E_{R/S}(t)$ is stated as:

$$\begin{aligned} S_{R/S}^{FTIR}(\tau) &\propto \int_{\Delta T} [\frac{1}{2}E_{R/S}(t) + \frac{1}{2}E_{R/S}(t-\tau)]^2\mathrm{d}t \\ &= \int_{\Delta T} \frac{1}{4}[E_{R/S}^2(t) + 2E_{R/S}(t)E_{R/S}(t-\tau) + E_{R/S}^2(t-\tau)]\mathrm{d}t \end{aligned} \tag{2.4a}$$

The first and third term describe the background signal impinging on the detector. Taking into account that the integration time ΔT is much bigger than the delay τ, we

combine the two terms in S_{back}. The second term represents the delay-dependent interferogram and can be written as a time-domain convolution if we invert the time axis (denoted by an upper index minus):

$$\begin{aligned} S_{\text{R/S}}^{\text{FTIR}}(\tau) &\propto S_{\text{back}} + \frac{1}{2}\int_{\Delta T}[E_{\text{R/S}}(t)E_{\text{R/S}}(t-\tau)]\mathrm{d}t \\ &= S_{\text{back}} + \frac{1}{2}\int_{\Delta T}[E_{\text{R/S}}(t)E_{\text{R/S}}^{-}(\tau-t)]\mathrm{d}t \\ &= S_{\text{back}} + \frac{1}{2}(E_{\text{R/S}} \circledast E_{\text{R/S}}^{-})(\tau) \end{aligned} \tag{2.5a}$$

We neglect the delay-independent background term in the further treatment (see Disadvantages on page 22). From basic Fourier analysis, a convolution in the time-domain corresponds to a multiplication in the frequency-domain. The inverted time axis results in the complex conjugate of the spectrum. Therefore, the Fourier-transform of Equation 2.5 results in the frequency domain signal:

$$\widetilde{S}_{\text{R/S}}(\omega) = \mathcal{F}\{S_{\text{R/S}}(\tau)\} \propto |\widetilde{E}_{\text{R/S}}(\omega)|^2 \tag{2.6}$$

After acquiring a reference and a sample scan, the sample response function is calculated via the ratio:

$$\frac{\mathcal{F}\{S_{\text{S}}(\tau)\}}{\mathcal{F}\{S_{\text{R}}(\tau)\}} = \frac{|\widetilde{E}_{\text{S}}(\omega)|^2}{|\widetilde{E}_{\text{R}}(\omega)|^2} = \frac{|\widetilde{E}_{\text{R}}(\omega)|^2 \cdot |\widetilde{H}(\omega)|^2}{|\widetilde{E}_{\text{R}}(\omega)|^2} = |\widetilde{H}(\omega)|^2 \tag{2.7}$$

Therefore, spectral information of the sample absorption can be obtained from the amplitude of the complex response function retrieved from two subsequent scans with the FTIR spectrometer. However, it does not provide dispersion (i.e. phase) information on the sample. This can be solved by using a dispersive FTIR spectrometer setup, where the sample is placed in one of the interferometer arms and the phase information is therefore measured.

Advantages

The FTIR spectrometer is well-established in infrared spectroscopy, because it is simple and robust. Moreover, it can be operated with incoherent light from a thermal source, because temporal coherence necessary for interference is introduced by

the beam splitter. Thereby, the two interferometer beams can interfere even if the source emits temporally incoherent light. Thermal sources have the advantage of being cheap and small, combined with a broad spectral coverage.
When operating FTIR spectrometers with noisy room-temperature detectors, they can still produce high-quality spectra because of two advantages:

- Fellget
- Jaquinot

Fellget's advantage refers to that multiplexing improves the signal-to-noise ratio (SNR) of the measurement if the detection is limited by detector noise. The reason is that all wavelengths of the incident light are detected simultaneously. Therefore, the SNR for a given measurement time is improved, e.g., compared to monochromators [21][22]. This is particularly important in the MIR range, where MCT detectors exhibit bad noise figures.
Jaquinot's advantage states that interferometric spectroscopy can provide a higher light throughput than for example monochromators. The maximum aperture in interferometers is limited by the mirrors as opposed to narrow slits employed for high resolution in monochromators [22][23].

Disadvantages

In time-integrating detection, the excitation field is measured together with the sample signal at all times. Therefore, Fourier-transform spectrometers are affected by the technical intensity noise of the excitation field in a delay-independent way. To avoid these noise limitations, additional methods like fast scanning or balancing can be employed [16][24][25][26].
Moreover, state-of-the-art MIR detectors suffer from dynamic-range limitations caused by saturation [4]. For samples with high absorption coefficients, all spectral components of the source can be absorbed preventing quantitative conclusions on the sample. This prevents scaling of the MIR power, which would improve the sensitivity and the range of measurable absorption. With higher MIR power, samples with high interaction cross section or large sample concentration can be analyzed and the sensitivity is increased as more sample molecules can be excited.

To conclude, Fourier-transform spectroscopy, e.g., employing FTIR spectrometers, have many advantages for example the possibility to use thermal sources. Employing an FTIR spectrometer, it is possible to measure absorption spectra of a great variety of samples ranging from proteins in the condensed phase to trace gases. Nevertheless, they suffer from limitations related to the dynamic range and noise figures of MIR detectors.

2.2.2 Field-Resolved Spectroscopy

In order to circumvent limitations of FTIR spectrometers resulting from noisy detectors and the time-integrating nature of the technique, we employ field-resolved spectroscopy. We achieve field resolution via EOS [14][27]. In the following section, the basics of EOS and the benefits for sensitive gas-phase spectroscopy are discussed.

Electro-Optic Sampling

Figure 2.4 shows a schematic of a typical EOS setup. Here, a sample waveform and a short gate pulse are temporally and spatially overlapped and focused into a nonlinear crystal, where the polarization of the gate pulse is changed due to the presence of the sample pulse. After recollimation, an ellipsometer is used to analyze the polarization state of the NIR light. The signal measured with the balanced diodes is proportional to the sample electric field. In our case, the frequency shift in the nonlinear crystal by the sample field is on the scale of the width of the gate pulse (see Equation 2.8). Because the resulting EOS signal is only contained in the spectral overlap region of the gate and SFG spectrum, the other frequency components of the gate pulse solely contribute to noise. Using a suitable short-pass filter SPF, these components can be removed to eliminate their noise contribution and improve the SNR of the measurement [28].

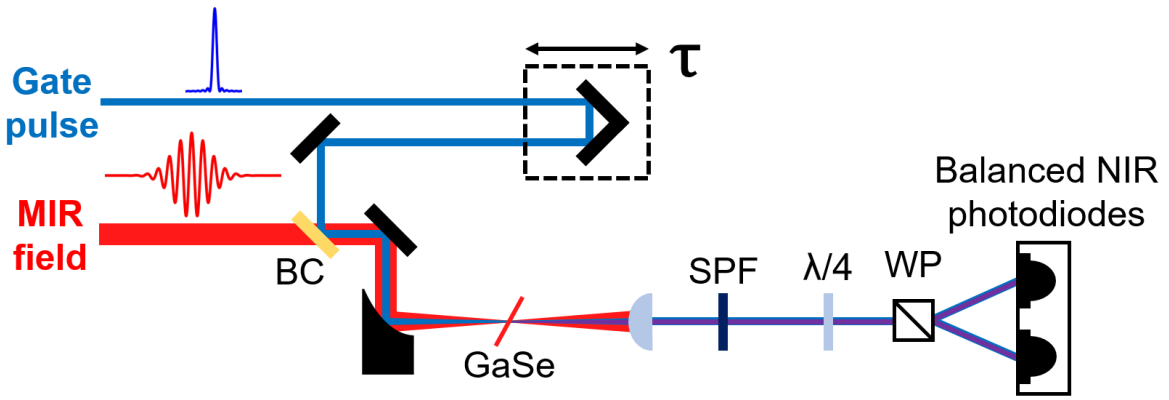

Figure 2.4: Electro-optic sampling setup for field-resolved spectroscopy. A variably delayed sub-MIR-cycle gate pulse is temporally and spatially overlapped with a MIR sample field at a beam combiner (BC). Both beams are focused into a nonlinear crystal (GaSe). The generated sum-frequency radiation cause a polarization change of the gate beam, which is measured by an ellipsometer setup, consisting of a quarter-wave plate, a Wollaston prism and balanced photodiodes. The short-pass filter (SPF) improves the SNR as gate photons only contributing to noise are filtered out.

For the MIR frequencies considered in this work, i.e., 20-41 THz, EOS is best described as a two-step process [27]. The second-order ($\chi^{(2)}$) interaction in a nonlinear medium is described as a combination of sum and difference frequency generation (SFG and DFG) [29]. For the thick detection crystals used in our experiments, mainly SFG is phasematched and we neglect the DFG terms [13]. In the first step, a $\chi^{(2)}$-process generates sum frequency components of the interacting NIR and MIR pulses. Taking only the mixing of three single frequency components into account, the SFG field E_{SFG} can be written in the frequency domain as [13][29]:

$$\widetilde{E}_{\mathrm{SFG}}(\Omega+\omega) \propto i\widetilde{E}_{\mathrm{gate}}(\Omega)\cdot\widetilde{E}_{\mathrm{sample}}(\omega) \tag{2.8}$$

with Ω and ω denoting the angular frequencies in the NIR and MIR regions of the gate and the sample electric field, respectively.
The second step includes the measurement of the generated sum-frequency radiation in a heterodyne detection scheme with the gate pulse acting as a local oscillator, resulting in a polarization change in their spectral overlap region. The change in the polarization is read out by an ellipsometer, consisting of a quarter-wave plate, a

Wollaston prism (WP) and two balanced photodiodes. If no sample field is present in the detection crystal, the angle of the quarter-wave plate is adjusted to generate circularly polarized light. Then, the intensities at the output ports of the WP are equal, resulting in a vanishing signal from the balanced photodiodes. A sample field at the detection crystal causes an imbalance at the detectors. By scanning the delay τ between gate and sample pulse, the time-domain sample electric field can be derived. The final balanced signal current ΔI from the photodiodes is proportional to the gate pulse intensity E^2_{gate} and the MIR field E_{MIR} [13]:

$$\Delta I \propto E^2_{\text{gate}} \cdot E_{\text{MIR}} \tag{2.9}$$

This allows to reconstruct the complete time-domain information of our sample field. Performing a calculation similar to that for FTIR spectrometry yields:

$$\frac{\mathcal{F}\{S_{\text{S}}(\tau)\}}{\mathcal{F}\{S_{\text{R}}(\tau)\}} \approx \frac{\widetilde{E}_{\text{sample}}(\omega) \cdot \widetilde{H}(\omega) \cdot \widetilde{A}_{\text{EOS}}(\omega)}{\widetilde{E}_{\text{sample}}(\omega) \cdot \widetilde{A}_{\text{EOS}}(\omega)} = \widetilde{H}(\omega) \tag{2.10}$$

The sample response function is multiplied to the MIR field and both spectra are multiplied by the spectral instrument response of EOS $\widetilde{A}_{\text{EOS}}(\omega)$. Therefore, we can measure the complex molecular response function $\widetilde{H}(\omega)$ with FRS.

Benefits over FTIR spectroscopy

Field-resolved spectroscopy mitigates limitations of time-integrating spectroscopy. The resulting signal scales with the sample field rather than the intensity (for a symmetric FTIR spectrometer) promising higher retrievable concentration dynamic range. Furthermore, we can temporally separate the molecular response from the strong excitation due to the time-gating of EOS. Therefore, the molecular response can be analyzed in the background-free wake of the excitation pulse with the detection noise floor given by the fundamental quantum noise of the gate pulse [4]. Thus, we circumvent the high intensity noise of the excitation, which enables higher sensitivity for FRS. Measuring the complete time-resolved trace of the sample electric field permits power scaling of the MIR field. This is possible if the MIR pulse duration is short enough compared to the free induction decay emitted by the molecules. The molecular signal of gas-phase samples extends over several tens of picoseconds and well into the nanosecond regime due to the narrow absorption linewidths [15]. Therefore, we can

measure their signal much longer compared liquids, promising higher resolution, as the molecular signal stays longer above the detection noise floor [2][30]. In general, the required resolution is application-dependent, but high resolution is needed in order to resolve the fine structure of all absorption bands to achieve high specificity [23][31]. Because the MIR field is upconverted into the NIR using SFG, low-noise semiconductors in the NIR can be used for detection. This is advantageous over MIR detectors, e.g., based on MCT [32].
The heterodyne detection process with the strong NIR gate pulse has two advantages: The phase information of the sample pulse stays preserved in contrast to a measurement of the SFG field itself [33]. Additionally, the SFG signal is amplified in order to be above the diode noise floor. This is advantageous when investigating weak SFG signals. The signal scales with the gate pulse intensity (see Equation 2.9), because the gate field generates the sum-frequencies and is used as local oscillator in the heterodyne detection scheme [34]. While heterodyne detection is not limited to the NIR range, dynamic range limitations of MIR detectors prevent improvements in this spectral region.
Although employing a nonlinear process in the detection setup, percent-level detection efficiency has been achieved by optimizing the EOS detection setup [13]. Harnessing all the advantages of FRS, we expect to enter a new sensitivity regime for gas-phase samples, combined with a broad spectral coverage and high detectable concentration range.

Field-resolved molecular signal

For field-resolved spectroscopy, we employ EOS to measure the excitation field of our laser source as well as the molecular response. To understand the results in Chapter 4, we have to clarify how such a sample reacts to a few-cycle MIR excitation pulse.
The MIR field hits the molecules inside our gas cell and excites vibrations and rotations. After excitation, the molecules emit coherent radiation with a well-defined decay time corresponding to the width of the absorption lines. The field amplitude of the response is proportional to the number of emitters, i.e., the concentration of sample molecules. Thus, a modification in the sample concentration changes the amplitude in the wake of the excitation pulse, accordingly. Due to the time-gating of EOS,

background-free measurements are possible after the excitation pulse has decayed. This implies a separation of the molecular signal from the strong excitation, which is one major advantage of FRS.

2.3 Enhancement Cavities

In addition to the maximized detection efficiency, the spectroscopic sensitivity can be increased by enhancing the signal from the molecular sample itself [13]. This may be achieved by elongation of the interaction path between MIR pulse and the sample gas. Possible approaches are multi-pass cells and enhancement cavities [16][17].
For multipass cells, propagating the sample beam between mirrors is usually feasible for path lengths of a few (tens of) meters. Path lengths of several meters require additional beam shaping optics to compensate the divergence of the beam. One possibility to implement this is a distributed waveguide, which, however, is space-consuming. Using a Herriott cell setup minimizes the amount of space needed, but can be tedious to implement for MIR light and large mirrors may be required.
Enhancement cavities provide an alternative solution to achieve path-length enhancement. As we have already seen before, we need a broad spectral coverage in the MIR to investigate complex samples. This creates challenges concerning dispersion management and the manner of coupling into the cavity. These challenges were addressed in previous works in our group [35] and the developed solutions are summarized in Chapter 3. In this chapter, the basic theory behind enhancement cavities is explained and relevant parameters are introduced.

Working Principle

Figure 2.5 shows a schematic of an EC in a bowtie configuration. Enhancement cavities are passive optical resonators because they do not comprise a gain medium. The input light (also called seed) is coupled into the cavity via an input coupler (IC), e.g., a partially transmissive mirror, and the cavity mirrors guide the beam back to the IC.

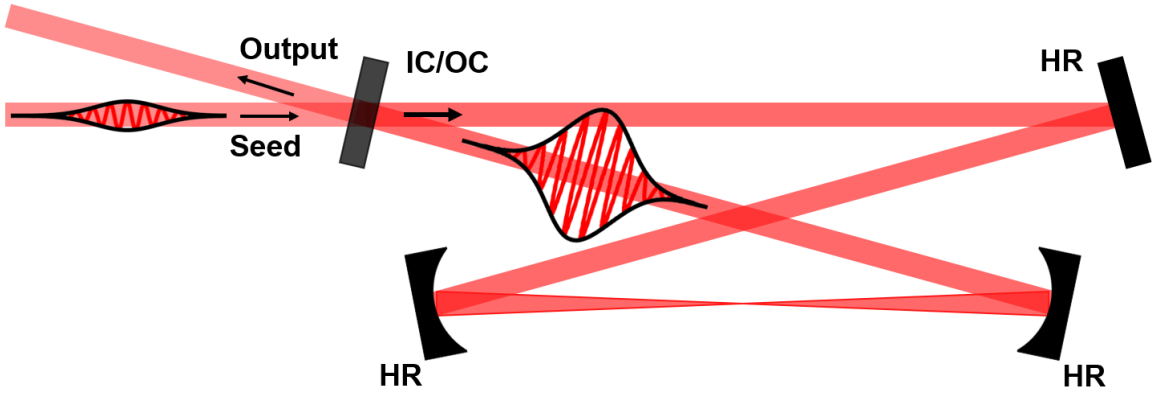

Figure 2.5: Schematic of an EC. The seed light is coupled in via an input coupler (IC). After one round trip using highly reflective (HR) mirrors, the light pulse in the cavity constructively interferes with the next incoupled pulse. Energy conservation requires destructive interference at the output after the output coupler (OC) of the cavity.

.

The light, which is reflected by the IC is called the reflected cavity beam. The cavity must be designed such that the stored pulse constructively interferes with the seed pulse towards the inside of the cavity. At the same time, both pulses destructively interfere at the output. The light, which leaves the cavity through the output coupler is called the transmitted cavity beam. High path-length enhancement can be achieved using this interference effect [36].
Relevant parameters to describe the cavity performance are the finesse $\mathcal{F}$, the power enhancement $\mathcal{E}$ and the effective path length L_{eff}, closely related to the path-length enhancement factor PEF. The circulating field E_C inside the cavity can be calculated in terms of a constant a, characterizing the cavity losses, and the round-trip phase ϕ [37].

$$E_C \propto \frac{1}{1 - a \cdot e^{i\phi}} \tag{2.11}$$

The resulting intensity as a function of the round-trip phase is plotted in Figure 2.6 and exhibits a 2π periodicity. The round-trip phase has a well-defined frequency relation. It is dependent on the light frequency, the transverse electromagnetic mode and the Gouy parameters [38]. Therefore, the qualitative behavior of the circulating intensity would be the same if plotted against the seed frequency. Figure 2.6 also illustrates the so-called free spectral range, which is the distance between two resonances. The ratio of the free spectral range and the full-width-at-half-maximum (FWHM) value $\Delta\phi$

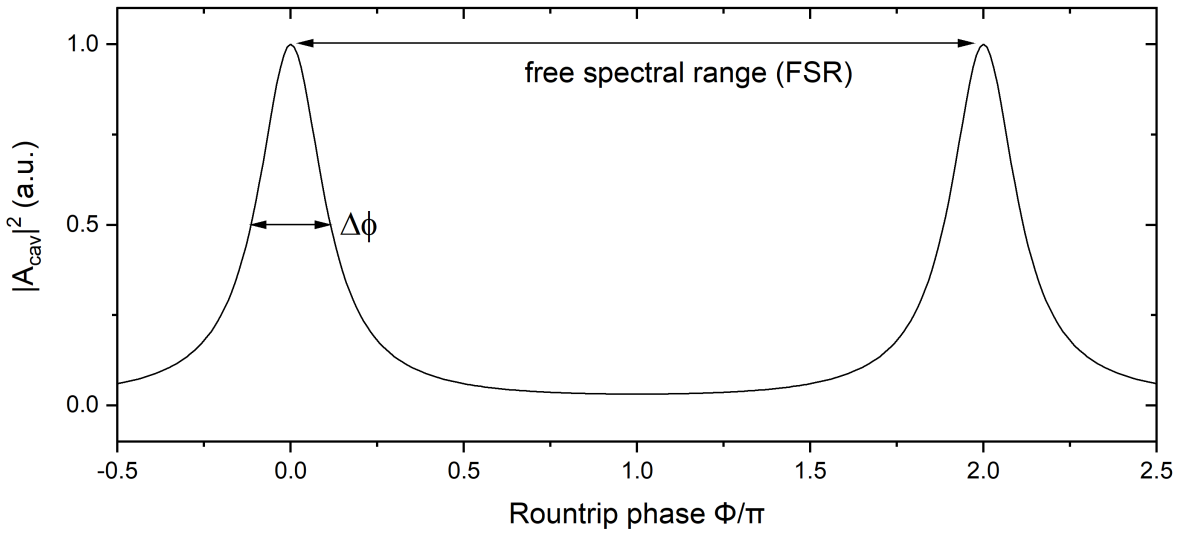

Figure 2.6: Circulating intra-cavity intensity plotted against the cavity round-trip phase ϕ. The distance between the two resonances is the free spectral range (in this case 2π). The full-width-at-half-maximum of a resonance is denoted as $\Delta\phi$. The intra-cavity signal shows the same qualitative behavior if plotted against the repetition rate of the seed light.

of the intensity resonances defines the finesse $\mathcal{F}$ of the cavity. The finesse depends on the losses by the IC reflectivity $R_{\mathrm{IC}}(\omega)$ as well as the power attenuation factor (per round trip) $R_{\mathrm{cav}}(\omega)$ and can be written as [38]:

$$\mathcal{F} = \frac{\pi(R_{\mathrm{cav}}(\omega)R_{\mathrm{IC}}(\omega))^{1/4}}{1-\sqrt{R_{\mathrm{cav}}(\omega)R_{\mathrm{IC}}}} \tag{2.12}$$

The power enhancement factor $\mathcal{E}$ defines the average optical power traveling inside the cavity. It is determined as the ratio between the intra-cavity power and the seed power. The maximum enhancement is achieved if the cavity is impedance matched. This means that the intra-cavity losses equal the IC transmission. In that case, no optical power gets reflected from the cavity [39]. However, $\mathcal{E}$ does not include the outcoupling of the intra-cavity power, which becomes important for applications, e.g., for high-sensitivity gas spectroscopy. Previous studies for FRS have shown that $\mathcal{E}$ is proportional to the path-length enhancement factor PEF, which is directly related to the sensitivity improvement for gas spectroscopy [35].
For absorption spectroscopy it is more convenient to express the enhancement by the

cavity in terms of an effective path length L_{eff} [39]. This parameter describes the path-length enhancement and relates it to an interaction length. This length corresponds to the equivalent single-pass path length through the sample, which would result in equal molecular signal strength. In general, the total path length L_{tot}, i.e., the interaction length with the sample, results from two contributions:

$$L_{\mathrm{tot}} = L_0 + L_{\mathrm{eff}} = L_0 + PEF \cdot L_{\mathrm{c}} \tag{2.13}$$

The length L_0 denotes the path length the beam travels through the sample gas outside the cavity and L_c the cavity length with a path-length enhancement factor PEF. The path-length enhancement quantifies the performance of the cavity compared to a situation without coherent superposition. The enhancement can be explained in two - effectively equivalent - ways: The first one is the effective path length, which models the enhancement as a longer interaction path given by the mean intra-cavity lifetime of the photons. On the other hand, the high intra-cavity power results in a stronger molecular signal, which can then leave the cavity via the output coupler.
Figure 2.7 illustrates the cavity properties with and without a sample gas for $L_0 = 0$. The discussion of Figure 2.7 a) is equivalent to the bowtie cavity seen in Figure 2.5. In Figure 2.7 b), a sample gas inside the cavity generates a temporally-delayed molecular signal. This molecular signal is visible in the reflection as well as the transmission.

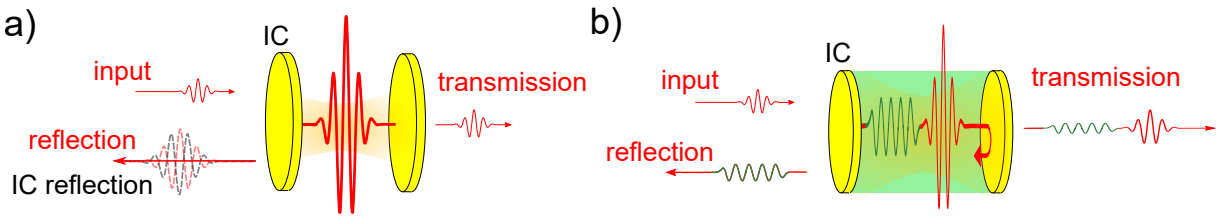

Figure 2.7: Illustration of an impedance-matched enhancement cavity a) without and b) with a sample gas. The input light gets reflected partially from the input coupler (IC) and interferes with the outcoupled intra-cavity signal. With a sample gas, the temporally-delayed molecular response is visible in both transmitted and reflected cavity trace. Drawing by P. Sulzer.

In conclusion, a passive optical resonator yields a powerful tool for spectroscopic path-length/sensitivty-enhancement. Designing an EC for broadband MIR waveforms can push the sensitivity limit further for linear absorption spectroscopy of gas-phase samples.

3 Experimental Work

In this chapter, the experimental work performed within the scope of this thesis is described. First, two gas-phase sample preparation protocols will be presented and verified. Then, the benchmarking work performed with an FTIR spectrometer is presented and the methodology is characterized. Similarly, the optical setup used for FRS combined with simulations for the experiments is presented. In the end, a novel MIR enhancement cavity setup is presented for the purpose of realizing a path-length enhancement over a broad spectral region.

3.1 Sample Preparation

In this work, two sample preparation protocols are introduced to prepare gas-phase samples. Reliable preparation of samples is important when investigating the sensitivity and detectable concentration dynamic range of optical setups experimentally. Otherwise no reliable conclusions about the linearity of the spectroscopic methods can be drawn. The samples comprise variable mixing ratios of acetylene, methanol and methane at different concentrations. Being a homo-nuclear diatomic molecule, nitrogen is IR inactive (see Chapter 2) and was therefore used as a carrier gas . For the protocols, the focus will be on accuracy and reproducibility of the prepared concentration.

3.1.1 Free-Expansion Protocol

To approach the topic of sample preparation, we start with the free-expansion protocol, based on the free expansion of gas into vacuum. Figure 3.1 depicts the setup used for this protocol. The setup includes two turbo pumps with appropriate pre-pumps to achieve the required high vacuum (typically $10^{-4}\,mbar$) to avoid background and

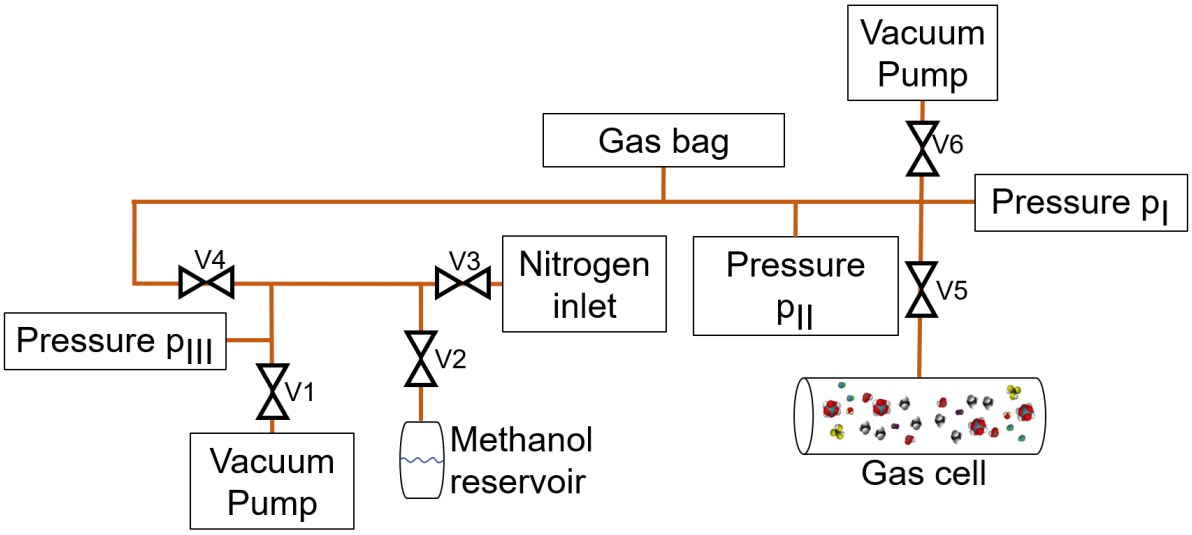

Figure 3.1: Vacuum setup used for the free-expansion protocol. Methanol vapor from the reservoir fills the evacuated gas cell. Afterwards nitrogen, as a carrier gas, is added to the gas cell. The gas bag is used for pressure balance. Dilution of the sample is achieved by free expansion of the sample into the evacuated system.

enable free expansion. Three measurement devices are used to record the pressure at different positions in the setup. All components are connected via copper tubes and stainless-steel adapters. The system can be partially divided by valves V1 to V6. For easier referencing, each volume is indexed with the valve numbers enclosing the corresponding volume.

Liquid samples at room temperature, such as methanol, need to be vaporized for the measurement. The following step-by-step instruction is for methanol but can be used for gaseous substances at room temperature by omitting the vapor-liquid equilibrium considerations (steps 3 and 4). In order to fill the gas cell with a methanol sample using the free-expansion protocol the following steps have to be performed:

1. Purge the tubes with pressurized air and nitrogen. Evacuate the tubes and flush them with nitrogen (repeat once).

2. Evacuate the setup (V2, V3 closed; V1, V4, V5, V6 opened).

3. Let methanol gas expand to the gas cell (free expansion). Wait until a pressure of p_I = 130 mbar is reached (vapor pressure of methanol at 20 °C) [40].(V1, V3, V6 closed; V2, V4, V5 opened).

4. Wait for approximately 30 s until the vapor-liquid equilibrium is obtained. Then close V2 and V5.
5. Evacuate the setup except for the gas cell and flush with nitrogen for cleaning purposes (repeat once). Evacuate the setup.
6. Fill V_{1256} with nitrogen at atmospheric pressure (V1, V2, V5, V6 closed; V3, V4 opened). Use the gas bag for pressure balance.
7. Open V5 for a few seconds until the sound of in-streaming nitrogen has vanished.

The final sample consists of the highest possible methanol gas-phase concentration as the saturation vapor pressure defines the maximum partial pressure of a substance at a certain temperature. That is at vapor-liquid equilibrium, which means equal evaporation rate and condensation rate. For smaller sample concentrations the following steps have to be executed after preparing the sample cell as described before:

1. Evacuate the setup except for the gas cell (V2, V3, V5 closed; V1, V4, V6 opened).
2. Open V5 and let the sample gas expand to vacuum (free expansion) (V1, V2, V3, V6 closed; V4, V5 opened).
3. Wait for approximately 30 s until an equilibrium is reached. Then close V5.
4. Perform steps 5-7 of previous list.

The free expansion of the stock solution and subsequent refilling with nitrogen leads to a concentration reduction with fixed ratio. This ratio can be calculated from the gas cell volume and volume V_{1236}. Performing these dilution steps iteratively leads to a steady decrease in concentration inside the sample cell.

Advantages

The free-expansion protocol is easy and straightforward to implement. It provides a good starting point for investigation of gas-phase samples at vapor pressure, the highest concentration possible in the gas phase. For methanol, the protocol provides reliable samples for percent-level concentrations.

Disadvantages

In particular for the preparation of low concentration samples problems arise with the free-expansion protocol due to the dilution process. With the dimensions and volume ratios of the setup employed here, it takes more than ten dilution steps until ppm-concentrations are reached. This is time consuming and increases the probability for deviations from the target concentration as contaminants can enter and at the same time sample molecules can leave the sample cell during the nitrogen refilling steps. These problems can be mitigated by refilling every second time, using the pump for dilution or by expansion into a bigger volume, but are not solved completely.
Furthermore, the high concentration inside the sample cell at the beginning is problematic. For methanol, adhesion plays a considerable role [41]. This hampers the dilution by a fixed factor as molecules sticking to the wall act as an unwanted source, which results in higher concentrations than expected particularly at the ppb level. An increased number of detached molecules can be caused by the nitrogen flow during pressure equalization. Potentially, the refilling can be omitted, but then saturation effects of the sample partial pressure are observed due to the decreasing pressure difference between sample cell and setup. The maximum pressure difference is limited by the minimum pressure achievable with the pumps. Expanding into a smaller volume in step 3 of the protocol circumvents high concentrations in the gas cell. However, preparing low concentrations is still time consuming.
Moreover, the preparation of sample mixtures is cumbersome. For variable mixing ratios at low concentrations, the preparation time can extend up to three hours. Therefore, this protocol will only be considered for single gas species.

To conclude, the presented protocol is very useful for high concentrations (0.5-13% for methanol) and yields a good starting point. Nonetheless, it is not flexible. Preparing different low concentration samples to investigate the sensitivity limits of the spectroscopic methods seems not feasible with this protocol. Therefore, another approach has to be used in order to prepare low concentrations accurately.

3.1.2 Injection Protocol

The so-called injection protocol circumvents limitations seen for the free-expansion protocol. Figure 3.2 depicts the setup.
A step-by-step description with all details of the protocol for laboratory use can be found in the appendix (see Chapter 5). It is written for liquid substances at room temperature but can be easily adapted for gas-phase substances. In summary, the protocol includes the following steps:

1. Inject a specific volume of liquid sample into an evacuated glass gas sampling bulb via a septum.
2. Fill the gas sampling bulb with nitrogen as carrier gas using the gas bag for pressure balance. The gas in the gas sampling bulb will serve as a stock solution.
3. Extract different volumes of stock solution with a gas tight syringe and fill it to the 250 ml gas syringe via a septum. The 250 ml syringe contains a pre-filled volume of nitrogen as carrier gas.
4. Transfer the sample to the evacuated gas cell. Pressure balance with the environment is provided via the gas syringe.
5. Close V5 and clean the rest of the system.

Performing these steps leads to a well-defined sample concentration inside the gas cell with total pressure equal to the atmospheric pressure. The concentration can be exactly calculated from the extracted sample volume and the volume of the gas sampling bulb and gas syringe. An example can be found in the protocol in the appendix. The relative error can be minimized by adjusting the concentration of the stock solution to the final concentration.

Advantages

Employing the injection protocol makes it possible to prepare percent-level down to low ppb-level concentration samples. The concentration can be varied by changing the extracted volume of stock solution. This makes it highly flexible for testing the sensitivity and achievable concentration dynamic range of the FTIR spectrometer and FRS. The extracted sample gas volume can be precisely controlled by the syringe

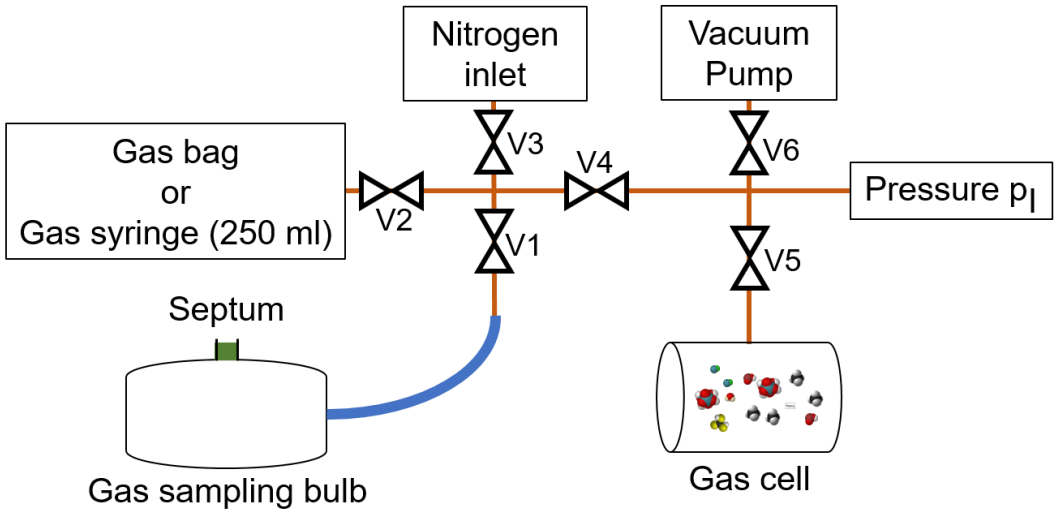

Figure 3.2: Vacuum setup used for the injection protocol. Specific stock solution concentrations are prepared in the gas sampling bulb by injection of well-defined sample volumes. Afterwards, the sample together with nitrogen as a carrier gas is prepared in the gas syringe and transferred to the gas cell. The gas bag guarantees pressure balance.

yielding high reproducibility (see Chapter 3.1.4).
The preparation time for low concentration samples is significantly reduced compared to the free-expansion protocol and all concentrations have the same preparation time (approximately 6 min). Furthermore, it is easily possible to prepare sample mixtures on the same time scale. The stock solution of each substance can be prepared independently. Then, we can inject the different sample gases with variable ratios to the gas syringe before filling the gas cell.

Disadvantages

Using the injection protocol, no vapor pressure samples can be prepared. This is prevented by the additional dilution step from the stock solution to the gas syringe even if the stock solution is at vapor pressure. Preparing slightly lower sample concentrations is feasible, but not very convenient because large stock solution volumes have to be extracted. Therefore, the free-expansion protocol is used instead to prepare high concentration samples.

In conclusion, the injection protocol yields reliable and flexible gas-phase sample preparation and it will provide the procedure used for most of the gas-phase measurement results. In addition to the preparation of methanol samples for testing sensitivity, gas mixtures can be prepared to demonstrate the specificity of our system.

3.1.3 Gas Cell

Two sample cells have been used throughout the experiments. A 15-cm-long gas cell was used for the FTIR spectrometer measurements. The length was limited by the sample compartment size of the commercial device. The second sample cell is 45 cm long and was fixed permanently in the FRS setup to preserve optimized alignment of EOS detection. Both gas cells consist of a stainless-steel tube with ZnSe windows fixed to the ends. In the case of the FRS cell, the windows are wedged in order to avoid additional background in the time trace due to multiple reflections.
The concentrations specified in Chapter 4 correspond to the partial pressure of the sample gas. The FTIR spectrometer measurement cell was directly filled using the previously described protocols. For simplicity, the FRS samples were also prepared in the short cell and then transferred to the evacuated cell inside the FRS setup. The partial pressure decreases due to this additional dilution step, which was accounted for in the concentration value for FRS. To obtain the same total pressure in both cells, nitrogen has to be filled to the FRS cell up to ambient air pressure. However, the nitrogen contained contaminants visible in the spectrum of the molecular signal of FRS. Therefore, the samples for FRS had to be measured at lower total pressure (p = 84 mbar) to avoid contamination. This affects the widths of the absorption lines and changes dispersion of the sample beam path. The resulting group delay was compensated for the time delay of the gate pulse. The contaminants did not influence the FTIR spectrometer measurements because the sensitivity is not high enough (see Chapter 4).
To ensure that the sample cell is not contaminated after preparation by a leak, we investigated the tightness of the small cell. Therefore, it was evacuated and we recorded the pressure evolution, which is shown in Figure 3.3. The pressure monotonically increased from 0.1 mbar to 2.5 mbar during 1.5 hours. After 14 hours, the pressure was 3.2 mbar. There was in-streaming air via a leakage, but the pressure evolution indicates sufficient tightness of the sample cell for pressures in the mbar range. Dur-

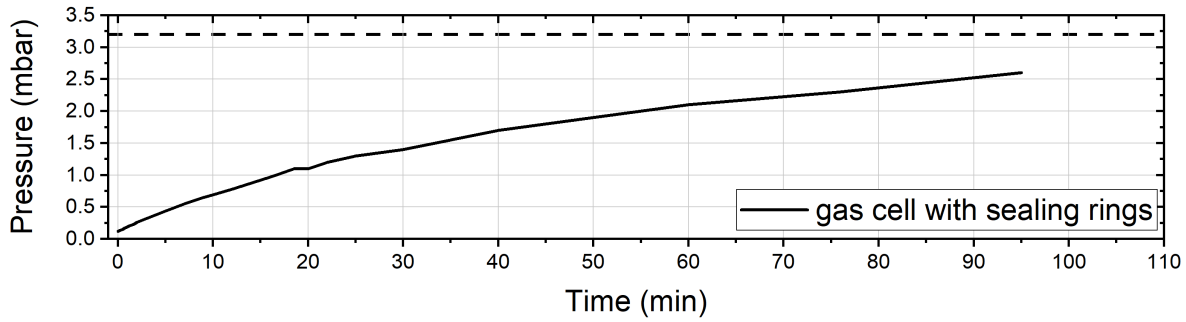

Figure 3.3: Pressure evolution of the evacuated gas cell using only sealing rings for tightening the windows. The dotted line shows the measured pressure after 14 hours, which indicates sufficient tightness for the gas handling.

ing preparation of the samples, the pressure was only at sub-mbar levels for a few minutes. Afterwards the gas cell was at atmospheric pressure, which makes gas exchange and therefore contamination negligible on the time-scale of our measurement, which was verified with the absorption spectra of the FTIR spectrometer.

3.1.4 Reproducibility

A crucial point for the measurement campaign is the reliability and the accuracy of the sample preparation. Therefore, we investigated the reproducibility of the sample handling process in detail.

We prepared 659 ppm of methanol with the injection protocol in the small gas cell and retrieved the concentration with the FTIR spectrometer. Then, the sample was filled to the FRS gas cell, resulting in a concentration of 61 ppm. After measuring with FRS, we measured the same sample with the FTIR spectrometer again. This procedure was repeated five times to gain information about the fluctuations of the sample handling.

Figure 3.4 shows the results of this analysis. The differently-colored dots represent the retrieved concentration for five different samples. Each sample was analyzed by the FTIR spectrometer directly after preparation. Then, after an FRS scan, the same sample was investigated by the FTIR again. The retrieved mean values of FRS and FTIR spectrometer are in good agreement with the expected values. However, the concentrations are smaller than the nominal values. Adsorption can cause this devia-

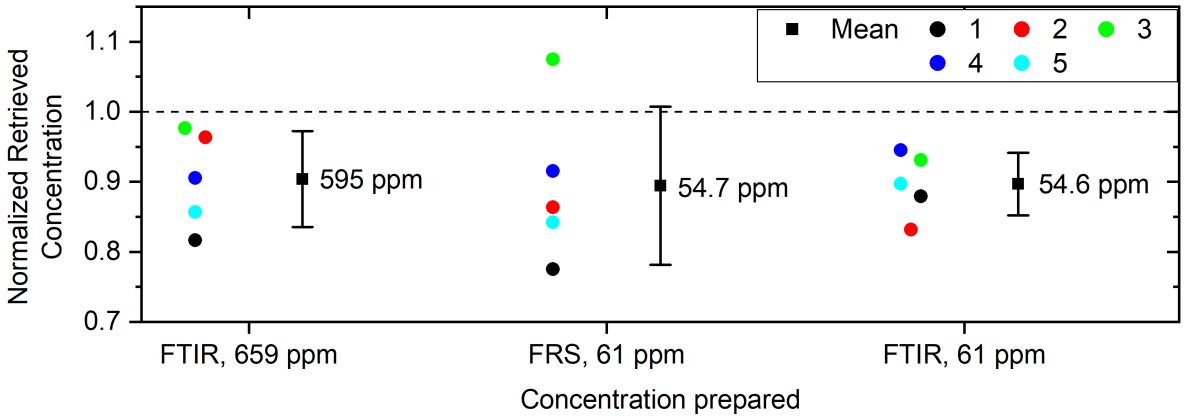

Figure 3.4: Reproducibility of the gas-sample handling. The differently-colored dots represent the retrieved concentration for five different samples. The black dots denote the mean values of the five scans with the standard deviation. The dashed line represents equal retrieved and prepared concentration. Smaller mean values than expected were retrieved. The results show sufficient reproducibility for the gas-phase experiments.

tion. It was already confirmed that adsorption has a relevant impact for stainless steel tubes [41]. The number of molecules adsorbed normalized to the molecule number in the sample cell is higher for smaller concentrations [42]. This will be relevant for the dilution series (see Chapter 4). The FRS data points show higher fluctuations than the FITR values. Most probable, the more complex data processing for FRS causes these deviations (see Chapter 3.3.1). The results indicate that the gas handling does not introduce considerable errors.

In conclusion, the sample handling reproducibility is sufficient for the purposes of this thesis. The different sample concentrations can be prepared with approximately 11 % relative deviation from the mean value.

3.2 Fourier-Transform Infrared Spectrometer

The current gold standard in broadband infrared spectroscopy are FTIR spectrometers. Therefore, the protocols described previously were validated by analyzing differ-

ent sample concentrations with an FTIR spectrometer. Furthermore, this state-of-the-art device will be used to benchmark the sensitivity and dynamic range for gas-phase samples. This will help us put the results obtained with FRS, as well as the further potential of the method into the context of the technological state of the art. In this section, the FTIR spectrometer used for these measurements is briefly described. Afterwards, the concentration retrieval is discussed.
The gas-phase experiments were conducted with a commercially available FTIR spectrometer (Bruker, Vertex 70). The beam path resembles the Michelson type setup shown in Figure 2.3. A thermal source provides MIR radiation with $P_{\mathrm{MIR}} \approx 4.7$ mW of optical power in the sample compartment. The gas cell was placed inside this compartment and connected to the vacuum setup. For detection, a liquid-nitrogen-cooled MCT detector was chosen as it provides better noise performance than standard room-temperature detectors. The total scan time defining the noise level was 60 s. The resolution for all scans was 1 cm^{-1}.
For all concentrations, the FTIR spectrometer acquired a reference scan for an evacuated gas cell prior to the sample measurement. After that, we prepared the sample and transferred it to the gas cell to perform the sample scan. The time between reference and sample scan was minimized to less than 30 s to avoid negative effects from thermal drifts.

Concentration Retrieval

To determine the concentration of the measured absorption spectra by the FTIR spectrometer, they were compared to reference data. The reference for methanol was taken from the Pacific Northwest National Laboratory (PNNL) IR database (`https://www.pnnl.gov/`) [43]. This absorption spectrum was measured for 1 m interaction path length and a concentration of 1 ppm. For simplicity, predominantly the maximum absorption from the Q-branch is considered here. The absorption value of the Q-branch at wavenumber $\widetilde{\lambda}$ = 1033 cm^{-1} is A_{PNNL} = 0.00112. The expression for the absorbance A reads $A = \epsilon \cdot L \cdot c$, where ϵ is the wavenumber dependent molar attenuation coefficient specific for a molecular sample [44]. The interaction length is

denoted with L and the sample concentration with c_{meas}. Using the absorbance A, of the measured sample, we can directly retrieve the concentration via

$$c_{\text{meas}} = \frac{A \cdot L_{\text{PNNL}} \cdot c_{\text{PNNL}}}{A_{\text{PNNL}} \cdot L} = \frac{A \cdot 1m \cdot 1ppm}{0.00112 \cdot L} \tag{3.1}$$

It is crucial that the baseline of the measured absorption spectrum is zero. Otherwise, the absorbance value yields wrong results. An appropriate spectral region was chosen to correct the baseline by a constant offset. The range from 2500 cm^{-1} to 2600 cm^{-1} is ideal, because common contaminants such as water vapor and carbon dioxide do not absorb in this region [45].

3.3 Field-Resolved Spectroscopy

After the benchmarking experiments with the FTIR spectrometer, we investigated the performance of FRS for gas-phase samples experimentally, e.g., methanol, because it has absorption lines at the maximum intensity dynamic range position of our instrument. As described in Chapter 2, field-resolved spectroscopy mitigates the limitations of the FTIR spectrometer, e.g., high intensity noise of the excitation field and modest noise figures of MIR detectors. The potential of FRS was already demonstrated for liquid-phase samples [4]. Analyzing gas-phase samples in conjunction with novel technologies with high spectral resolution, especially frequency combs, enables high specificity due to the longer coherence time of the resonant emission of gases compared to liquids [11]. In this chapter the optical setup used for FRS is illustrated. Then, the data acquisition and post-processing as well as the simulation of the molecular response using the high-resolution transmission molecular absorption (HITRAN) database is explained.

Figure 3.5 shows the setup used for the gas-phase FRS measurements (details in [18][13]). An erbium fiber oscillator is frequency-shifted and seeds two stages of amplification in thulium fibers (see Figure 3.5 a)) [47]. The resulting pulses have 50 W of average power with 250 fs FWHM pulse duration at a center wavelength of 1965 nm. These pulses are split into two channels. Each channel contains a photonic crystal fiber for nonlinear self-compression. The channel with the PCF 2 compresses the pulses down to 13 fs, which will be used as the gate pulse later. The other channel compresses the pulses to 32 fs duration. Afterwards these compressed pulses

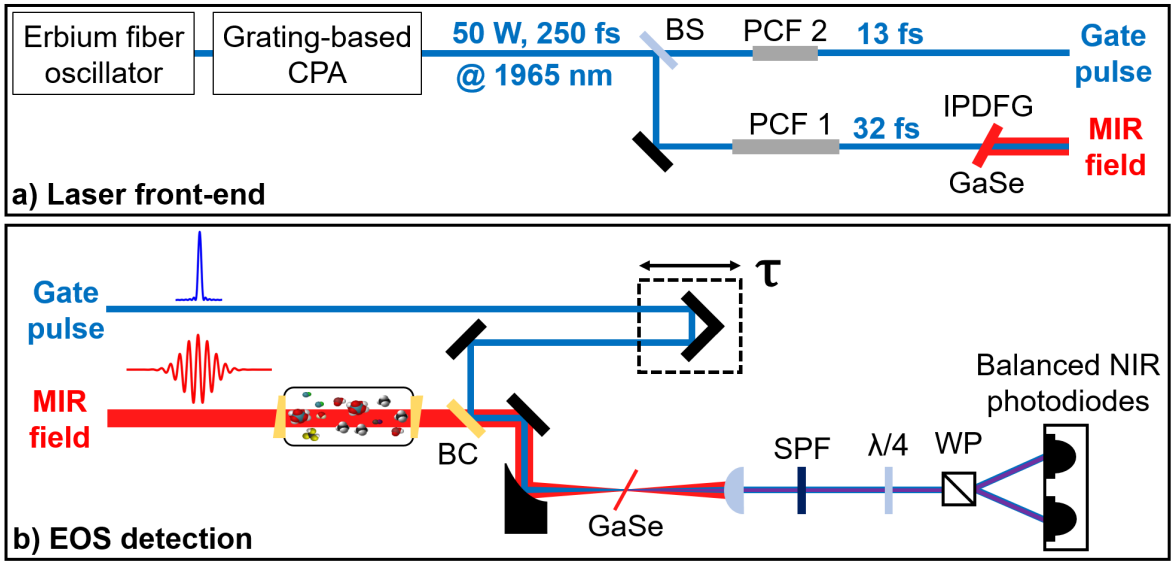

Figure 3.5: Optical setup used for the FRS measurements. All components can be placed in a vacuum environment. The output of an Erbium fiber oscillator is amplified by a grating-based chirped pulse amplification (CPA) setup. A beam splitter (BS) sends the amplified pulses to two photonic crystal fibers (PCF) for nonlinear self-compression. One channel serves as a gate pulse and the other channel is used for MIR generation via intra-pulse difference frequency generation (IPDFG) in GaSe. The MIR is separated from the driving NIR beam via a grating-based long-pass filter (not depicted) [46]. The EOS detection scheme was explained in detail in Chapter 2. The sample field is sent through the gas cell containing the sample molecules via ZnSe windows before combination with the gate pulse by a ZnSe beam combiner (BC).

drive intra-pulse difference frequency generation (IPDFG) in a GaSe crystal to generate MIR light centered around 30 THz frequency with 80 fs pulse duration. Compared to thermal MIR sources, the generation of MIR light via IPDFG results in spatially and temporally coherent light. Additionally, the brilliance exceeds that of thermal sources or large-facility synchrotrons [18]. The MIR spectrum spans from 19.6 THz to 41.1 THz at the -30-dB-level. This broad coverage benefits the characterization of complex molecular ensembles.

The detection scheme (see Figure 3.5 b)), described in detail in Chapter 2, is extended by the gas cell (length l = 45 cm) in the MIR beam path. After transmission through the sample cell the MIR beam is overlapped with the gate pulse using a ZnSe plate at Brewster's angle. Then, a parabola focuses both beams into a GaSe crystal. An

ellipsometer analyzes the resulting signal from the crystal (see Chapter 2). The difference current from the balanced InGaAs photodiodes is amplified by a transimpedance amplifier and processed by a LabVIEW program. Using the mechanical stage, a variable delay τ is introduced, which enables a temporal scan of the gate pulse over the sample field. Currents are measured as a function of this delay. The measured traces are proportional to the sample field, with differences arising from phasematching, the gate pulse duration and spectral post-filtering [13].

3.3.1 Data Handling and Processing

This section briefly summarizes the main post-processing steps for the data acquired using EOS. First, all real-valued time-domain traces are interpolated on the same evenly spaced time axis. The zero position of each trace was determined by the position of the peak value and the two neighboring zero crossings. The first trace is taken as reference and the remaining curves are shifted accordingly. Afterwards the time position of the traces is adapted such that the traces have maximum overlap. Thereby, time delay fluctuations were compensated, e.g., from errors in the delay value provided by the mechanical stage.
Next, the traces are multiplied by a factor to adjust their field amplitude compared to the reference trace. This is valid as there are several sources for a change in signal strength, e.g., the MIR power sent to the EOS detection or beam pointing fluctuations. In the end, each data set is split into two equal-sized sets. One output file contains the average of the first half and the second file the average of the second half of the data set. This is necessary to estimate the noise floor from the difference between two reference measurements, which determines the limit of detection (LOD) for FRS. Using the Hilbert-transform, the complex envelope of the pre-processed average traces is calculated.[1] The complex envelope has the same information content as the physically real electric field, but it simplifies data interpretation and handling.

3.3.2 HITRAN Simulation

In order to exploit the time-gating advantage of FRS, a different method for the concentration retrieval as compared to the time-integrating FTIR spectrometer measure-

[1] The python library used for these calculations and the simulation were written by M. Högner

ments is beneficial. Therefore, the sample response in the wake of the few-cycle pulse is simulated in the time domain. To achieve this, we used the HITRAN line data base via the HITRAN Application Programming Interface [45]. The input data set contains the total pressure, fraction and molecule type of the sample as well as the temperature and the line profile. Using the line data downloaded from the HITRAN data base, complex-valued Lorentzian-shaped absorption lines were computed with the correct strength, line width and spectral position corresponding to the laboratory conditions. These absorption lines are then combined in the complex absorption coefficient $\widetilde{\alpha}$. Afterwards, the sample response can be calculated using Beer-Lambert's law with gas cell length L and reference spectrum $\widetilde{E}_{\text{ref}}(\omega)$ (measured with an empty sample cell) [44].

$$\widetilde{E}(\omega) = \widetilde{E}_{\text{ref}}(\omega) \cdot e^{-\widetilde{\alpha} \cdot L/2} \tag{3.2}$$

As the calculation is performed with complex envelopes and absorption coefficient rather than intensities, the phase information stays preserved. After computing the Fourier-transform of $\widetilde{E}(\omega)$, the measured traces can be time filtered and $\widetilde{\alpha}$ can be adjusted to the measured spectral signal via the concentration.

3.4 Enhancement Cavity

Employing an EC together with FRS can push the sensitivity limit for gas-phase samples further. The challenge is to achieve broadband enhancement to investigate molecular ensembles. In this chapter, the experimental setup and work conducted with an ultra-broadband EC will be described. Possible cavity designs, including the one presented here, have already been explored thoroughly in our group [35][48]. Therefore, a brief summary will be given and we will then focus on the application for gas-phase experiments.

Figure 3.6 shows the experimental setup for the cavity experiments. The same MIR source, used for the single-pass experiments and described in detail in Chapter 3.3, is used for the EC experiments. A motorized flip mirror in front of the single-pass gas cell (see Figure 3.5) sends the MIR beam to the vacuum chamber containing the cavity. Wedged ZnSe windows separate the cavity chamber to be able to prepare a well-defined sample concentration inside the chamber. Before and after the cavity, the beam travels a length $L_0 = 6.55\,m$ with sample interaction. Two concave

mirrors (f=15 cm and f=25 cm), under small angle of incidence, serve as a telescope to achieve mode-matching of the input MIR mode to the eigenmode of the cavity.

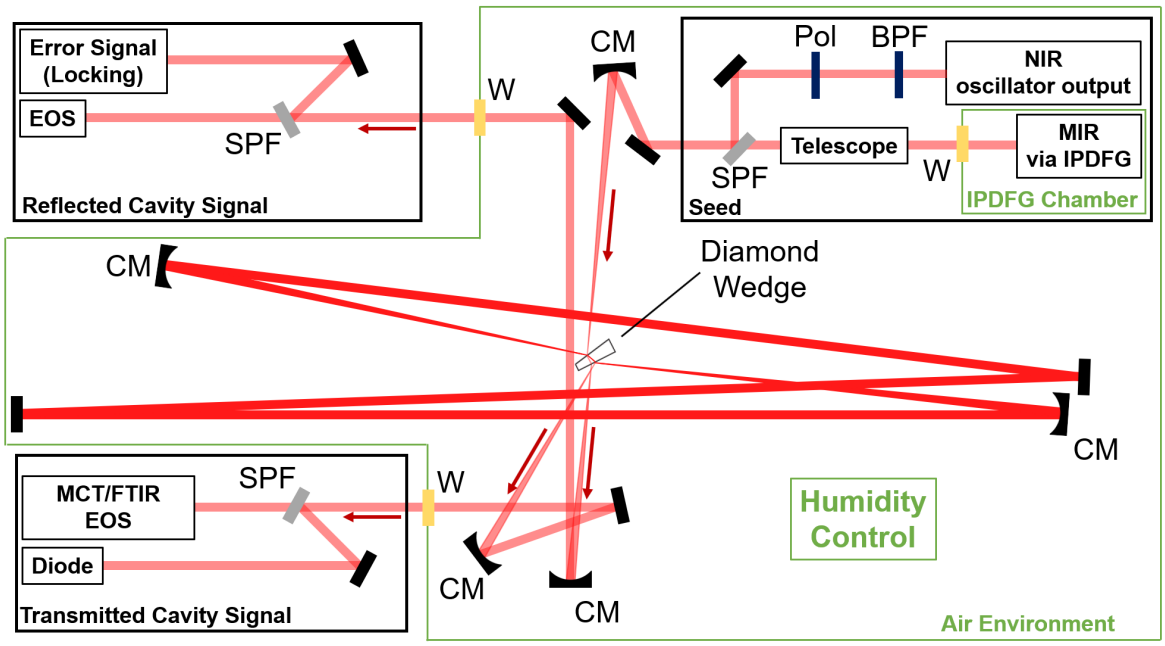

Figure 3.6: Setup sketch used for the gas-phase experiments with an ultra-broadband EC in a nitrogen environment separated by ZnSe windows (W). The same MIR source as for the single-pass experiments and additionally the 1550 nm output of the oscillator were used as a seed. The NIR light is filtered by a band-pass filter (BPF) and the polarization is adjusted by a polarizer (Pol). The MIR light passes a telescope for mode-matching and is then combined with the NIR light using a short-pass filter (SPF). After the SPF, both beams are focused by a concave mirror (CM) and then enter the cavity via the diamond wedge. The NIR reflected cavity signal is used to create an error signal for locking. Using a SPF, the reflected MIR beam can be analyzed by EOS. The transmitted beams are sent to a diode and an MCT detector, respectively, to visualize the cavity resonances on an oscilloscope. An FTIR spectrometer and EOS is employed to investigate the transmitted MIR beam.

An auxiliary beam for locking to the cavity length is derived from the fundamental frequency comb generated by the Er:fiber laser oscillator. This beam is coupled into a fiber and then fed through a vacuum-tight connector into the chamber. After collimation, a polarizer selects the p-polarized component, because of the cavity design with a reflective input coupler close to Brewster's angle. A band-pass filter selects spec-

tral components, which create NIR resonances at the MIR resonance position used for locking. Afterwards, both beams are recombined with a germanium plate and focused into the cavity. The focal position corresponds to the focus point of the curved cavity mirrors to achieve mode-matching.
Previous works have shown that broadband enhancement can be best achieved using reflective input coupling by a diamond wedge [35][49]. Using a wedge eliminates unwanted effects, e.g., the etalon effect. Such a thin diamond wedge (mean thickness 350 $\pm$ 50 µm) is placed close to Brewster's angle inside the cavity to minimize intra-cavity losses for p-polarized light. For optimum enhancement, the wedge angle must be chosen such that the cavity is impedance matched. For the results presented in this work, this angle is 1° with a measured spectrally averaged MIR IC reflectivity of 4.3 %. The cavity itself is in a bowtie configuration with unprotected gold mirrors, which have a flat spectral phase over more than 15-150 THz frequency range and therefore do not limit the dispersion management [35][50].

For characterization of the cavity either the electro-optic signal recorded after reflection or transmission through the cavity are analyzed. In the case of reflective input coupling, the transmitted seed beam corresponds to the reflected cavity beam as it does not enter the cavity. Due to the wedge, the transmitted cavity beam can be separated from the reflected beam (see Figure 3.6). A concave mirror recollimates each of these beams and a germanium plate splits the MIR from the NIR light. The transmitted NIR and MIR light is sent onto an MCT and InGaAs detectors, respectively.
To visualize the cavity resonances on an oscilloscope (see Figure 3.7 b)), the repetition rate of both pulse trains is varied linearly by sending a ramp voltage to an electro-optic modulator (EOM) in the fiber laser oscillator, resulting in a transmitted signal corresponding to the intra-cavity intensity plotted in Figure 2.6. The resonances of both beams are at comparable cavity length, because the round-trip phases show small differences due to similar complex refractive indices at both wavelengths [50][51].
The reflected NIR beam is used for locking the cavity to a length with maximum intra-cavity intensity using a polarization-based locking scheme originally proposed by Hänsch and Couillaud [52]. This scheme results in dispersion-shaped resonances as shown in Figure 3.7 a), which are used as an error signal. The error signal has its characteristic zero-crossing at the position of a NIR resonance and therefore serves as a feedback for locking of the oscillator repetition rate to the cavity length for max-

imum enhancement (see Chapter 2). Additionally, the free-running carrier-envelope offset (CEO) frequency f_{ceo} of the NIR oscillator is constant on the relevant time-scale of hours. As a result, the optical frequency f of a single mode of the frequency comb $f = f_{ceo} + N \cdot f_{rep}$ is locked[2]. Due to the MIR generation via DFG, the repetition rate of both pulses is identical and the carrier-envelope offset frequency f_{ceo} of the DFG comb is intrinsically zero.

Moreover, we have an additional degree of freedom for the MIR. Varying f_{ceo} of the NIR in locked position does not change the NIR cavity output signal as the EOM compensates the change in f_{ceo} via f_{rep} in order to guarantee constant optical frequency f. This change in f_{rep} affects the MIR resonance position as f_{ceo} is inherently zero. As a consequence, the MIR resonances are shifted against the NIR resonances. Consequently, changing of f_{ceo}, while cavity and NIR comb are locked, allows us to bring cavity and MIR modes in resonance.

[2]N denotes the mode number of the frequency comb

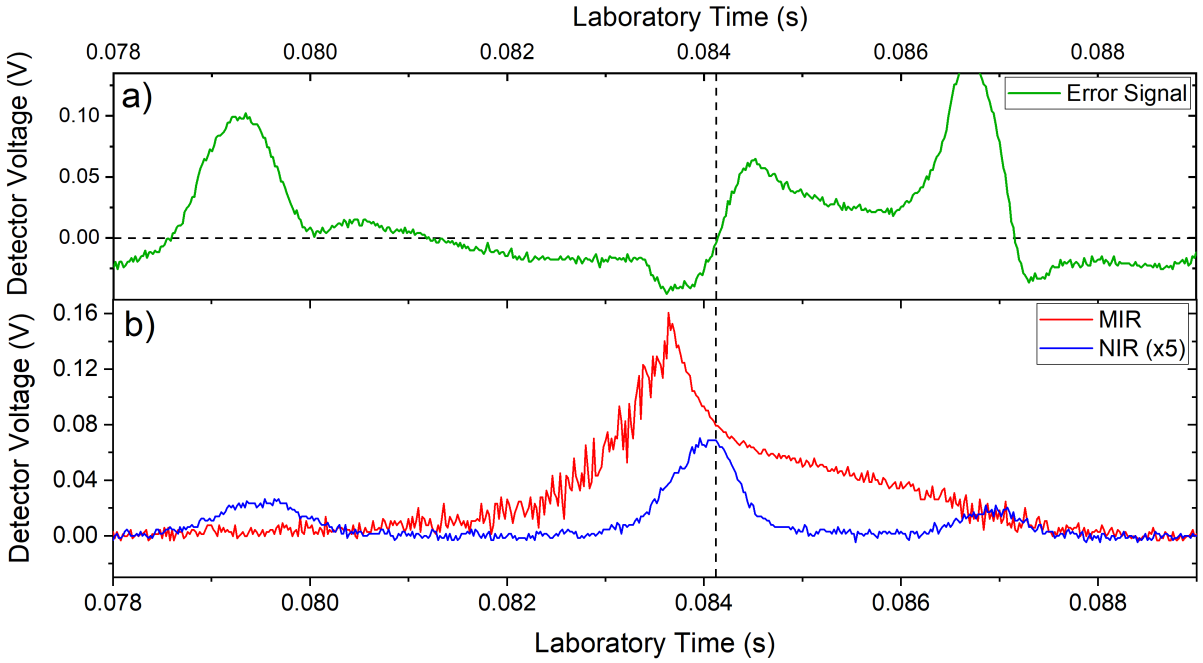

Figure 3.7: Detector voltages on the oscilloscope plotted against laboratory time. A ramp voltage is sent to the EOM of the oscillator such that the repetition rate is varied linearly corresponding to the time axis in this plot. a) Characteristic dispersion-shaped error signal obtained with the polarization-based Hänsch-Couillaud locking scheme. b) MIR and NIR resonances of the intra-cavity intensity. The zero-crossing of the error signal is at the position of a NIR resonance. The MIR resonance position was tuned by the carrier-envelope frequency for maximum signal.

The challenges for broadband enhancement have been thoroughly discussed in previous works in our group [35][53][54]. For broadband enhancement, the cavity parameters have to be controlled such that f_{ceo} is equal to the optimal offset frequency. As f_{ceo} of our MIR comb is inherently zero, the optimal offset frequency has to be set to zero [54]. This is done by changing the humidity inside the cavity chamber to vary the dispersion. By carefully regulating the humidity, we achieved ultra-broadband enhancement of the fundamental Gaussian mode. This was confirmed by analyzing the transmitted cavity beam profile using a MIR camera and the spectrum using an FTIR spectrometer. Being in a cavity configuration supporting the fundamental Gaussian mode has several advantages, e.g., easier mode-matching between the seed mode and the cavity eigenmode and higher enhancement [35].

The MIR resonance at a relative humidity of approximately 16 % is plotted in Figure 3.7. The shape of the MIR resonance is distorted by nonlinear effects in the MCT detector. Maximum spectral intensity in the MIR is obtained for the position indicated by the vertical dashed line. This configuration is employed during the gas-phase measurements using the reflected and transmitted MIR cavity beams with a locked cavity and FRS. The gas sample was filled to the cavity chamber in order to avoid additional transmissive cavity optics. We used methanol concentrations below 1 ppm as we expected a significant influence of dispersion induced by the methanol absorption resonance at 31 THz.

4 Experimental Results

In the previous two chapters, the theoretical background of infrared absorption spectra as well as techniques to retrieve the complex sample response function were presented. Two preparation protocols for gas samples were presented to investigate the performance of an FTIR spectrometer and FRS experimentally.
In this chapter, the experimental results obtained with these methods are presented. The FTIR spectrometer dilution series aims to validate the sample preparation and serves as a sensitivity benchmark for state-of-the-art FTIR spectroscopy. The determination of values for the LOD and the retrievable concentration dynamic range are the goal of these experiments. Using this benchmark for comparison, we performed a dilution series with FRS. Investigating the noise floor for different averaging times reveals the potential of FRS and indicates means of further improvement. Analyzing the time-domain molecular signal deepens our understanding of rotational-vibrational spectra and might open new avenues for future experiments. The experimental results of the broadband MIR cavity with gas-phase samples demonstrate one possibility for path-length enhancement and provide a proof-of-principle application.

4.1 FTIR Spectrometer Measurement Campaign

Dilution Series

The two goals for the measurements with the FTIR spectrometer are to validate the sample preparation protocols and to provide a benchmark for the field-resolved measurements. An FTIR spectrometer is ideally suited as it is well-established and versatile (see Chapter 2). It provides a good reference of state-of-the-art spectroscopy in terms of sensitivity and measurement dynamic range.
Methanol sample concentrations from 400 ppb to 12 % were prepared using the two

protocols described in Section 3.1. The resulting absorption spectra are analyzed to retrieve the concentration (see Chapter 3). Figure 4.1 shows the resulting comparison of the prepared and measured concentrations. To obtain the error bars at the boundaries of the detectable concentration range, each concentration was prepared five times and every sample was measured five times consecutively. The data point corresponds to the mean value of the resulting 25 independently retrieved concentrations. The y-error bars are the standard deviation of five consecutive scans

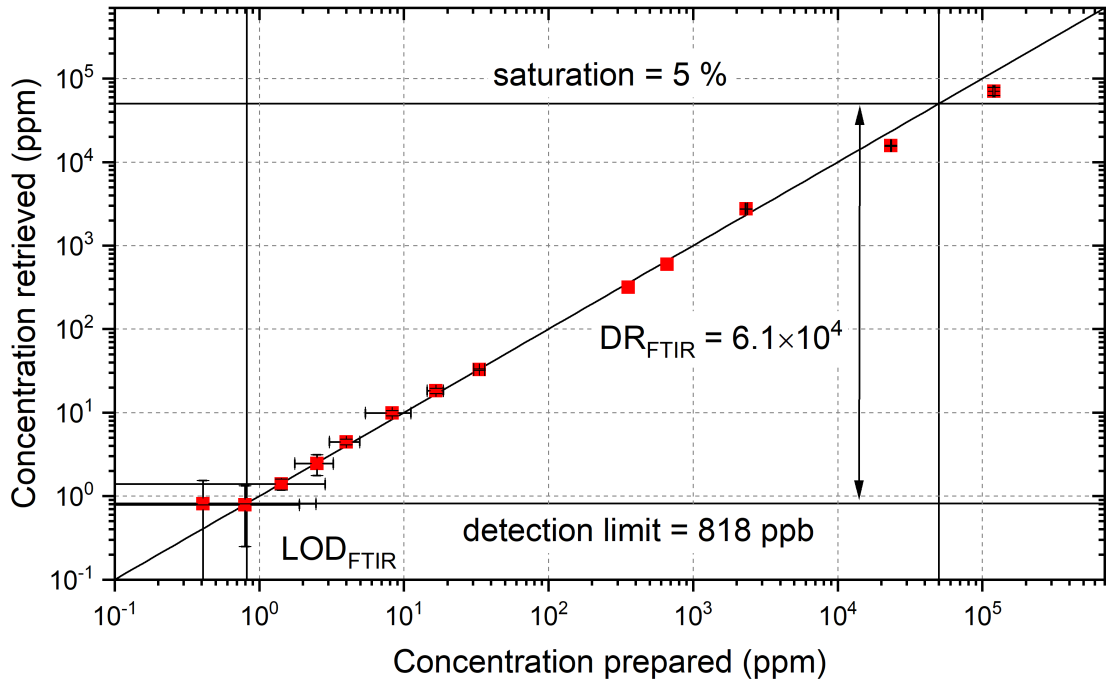

Figure 4.1: Methanol dilution series for the FTIR spectrometer measurements. The retrieved concentrations are in good agreement with the expected values, verifying the preparation protocol. The LOD was determined to be 818 ppb by the noise equivalent concentration of an identity scan. The maximum concentration for the CO-stretch mode of methanol is limited by saturation of the P-branch absorption at 5 % concentration resulting in 6.1×10^4 retrievable concentration dynamic range. The error bars at high concentrations are smaller than the data points.

of the same sample and the x-error bars are computed using five different samples prepared with nominally the same concentration. The retrieved concentrations are in good agreement with the identity curve.

At percent-level concentration, the absorbance values are smaller than expected, which can be explained by adsorption effects (see Chapter 3). For ppm-level concentrations, the absorption signal is comparable to the noise floor and the SNR is approximately 1, which increases the size of the error bar. These results, together with the reproducibility check in Chapter 3 validate the sample preparation protocol.
For benchmarking the sensitivity and retrievable concentration dynamic range, we use the CO-stretch band of methanol consisting of spectral features from 29 THz to 32.5 THz (see Figure 2.1). The results have to be linked to the averaging time and the interaction length with the sample to yield a fair comparison to FRS, which are 60 s and 14 cm for the FTIR spectrometer measurements, respectively. To determine the LOD, we measured two reference scans subsequently and treat one as the sample. This corresponds to a sample response function $\widetilde{H}(\omega)$ equal to unity. Theoretically, at all frequencies there should be no measurable absorbance. However, noise causes fluctuations of the absorption spectrum around zero. The root-mean-square of this signal was computed, and the corresponding (noise equivalent) concentration for methanol was determined to be 818 ppb and defined as the LOD of the FTIR spectrometer [4]. This corresponds to the measurement of a molecular signal with SNR of 1 in comparison to the average error of the zero-absorption line.
At lower concentrations (see 400 ppb data point) the molecular signal vanishes in the noise floor. At 5 % concentration, the absorbance value of the P-branch saturates preventing retrieval of higher concentrated samples. The data point at 12 % concentration was obtained by evaluating the first overtone of the CO-stretch mode at 2054 cm^{-1}. In principle, more spectral features can be used to determine the methanol content, but as specificity is one key aspect in applications, it is necessary to have high measurement dynamic range using only one spectral feature [23][31]. We find a dynamic range between the maximum retrievable concentration and the LOD of 1.5×10^5 using only the CO-stretch mode of methanol.
To put the limits obtained for the FTIR spectrometer into a perspective for applications, we can look at the abundance of typical biomolecules in the liquid phase. The measurement dynamic range already covers a large fraction of such biomolecules [55]. Therefore, it is possible to investigate them for potential health-state monitoring or disease detection [8][10]. Increasing the sensitivity enables investigation of a greater variety of biomolecules, which would push the usability for clinical applications further. Extending the analysis to the gas phase promises higher specificity due to the longer

coherence time of the resonant emission, which is crucial for biomedical applications [11][23]. Tools to create gas-phase samples out of liquid biomedical probes exist, but have their limitations [12].

4.2 FRS Measurement Campaign

Based on the sensitivity potential of FRS described in the previous chapters, which was already demonstrated in the liquid phase [4], we examined the performance of FRS in the gas phase. The results of a dilution series similar to the experiments with the FTIR spectrometer will be presented and compared to our benchmarking experiments. The intensity dynamic range at 30.9 THz of our laser source with FRS can be determined to $DR = 8.8 \times 10^{13}$ for 16 s of measurement time [13]. This promises an improvement in terms of sensitivity and concentration dynamic range. Moreover, the bandwidth of the laser source spans more than one octave (19.6-41.1 THz at the -30-dB-level). We investigated sample mixtures consisting of acetylene, methanol and methane, to demonstrate the potential of this broad coverage and to quantify the LOD for each molecular type. Increasing the averaging time to achieve higher sensitivity was analyzed. Moreover, we investigated the temporal evolution of the molecular signal, which opens conceivable avenues for future experiments to achieve higher sensitivity and specificity.

4.2.1 Dilution Series

In analogy to the dilution series (see Figure 4.1), sample concentrations from 2 ppb to 12 % were prepared and retrieved by FRS.[1] Figure 4.2 visualizes the time-domain traces for different sample concentrations. At high concentrations, the strong absorption changes the field envelope of the excitation pulse, visible in Figure 4.2 a). For a decreasing number of absorbers, the envelope converges to the reference curve. This evolution is reproduced by the simulation using the HITRAN line data [45]. In Figure 4.2 b) the envelope of the field amplitude of each scan decreases by a factor of approximately ten, corresponding to the change in concentration (see Section 2.2.2). For the lower concentrations, the amplitude merges with the noise floor at around

[1] The measurements were performed together with D. Gerz

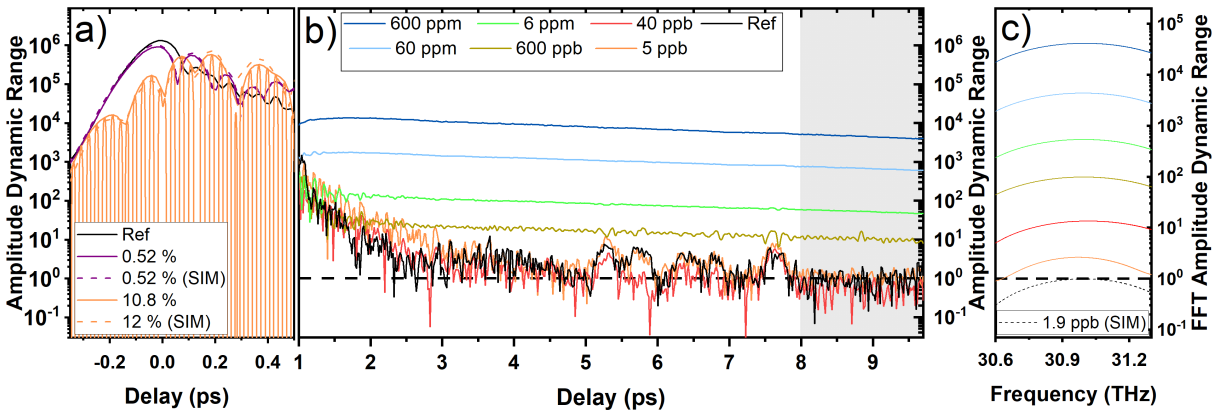

Figure 4.2: Time-domain traces of the dilution series. a) Excitation pulse and two percent-level samples showing the effect of high absorption on the pulse envelope of the field. The measured drop at the rising edge of the pulse can be reproduced by the simulation. b) Free induction decay of traces with varying sample concentration. The time window from 8 ps to 10 ps was used for filtering. c) Fourier-transform of the time-filtered signal. The peak values were used to determine the concentration for the dilution series.

3 ps, allowing for background-free measurements. The noise level is defined by the NIR gate pulse shot noise, but reveals background signals between 5 and 6 ps, as well as between 7.5 and 8 ps [13]. The origin of these features has not yet been clarified, but they most likely emerge from multiple reflections in optics. Therefore, the time window from 8 ps to 10 ps was chosen for further analysis. After Fourier transformation of the signal in this time window, we determined the concentration from the signal strength at 31 THz (see Figure 4.2 c)) using a simulation, which is described in Section 3.3.2. The peak amplitude decreases in accordance with the time-domain signal. The dotted line indicates the LOD of FRS.

Figure 4.3 shows the corresponding comparison of the prepared and measured concentrations. The retrieved concentrations are again in good agreement with the prepared values. Measurement and subsequent detection of the corresponding concentration was possible up to 12 %, limited by the vapor pressure of methanol [40]. The shaded areas in Figure 4.3 indicate whether the concentration is retrieved in the time (orange) or frequency domain (blue), respectively. Due to the large absorption of percent-level samples, the frequency domain signal saturates. For those concentrations, we therefore harness that with EOS we have access to the full time-domain

response to an impulsive excitation to retrieve the concentrations.

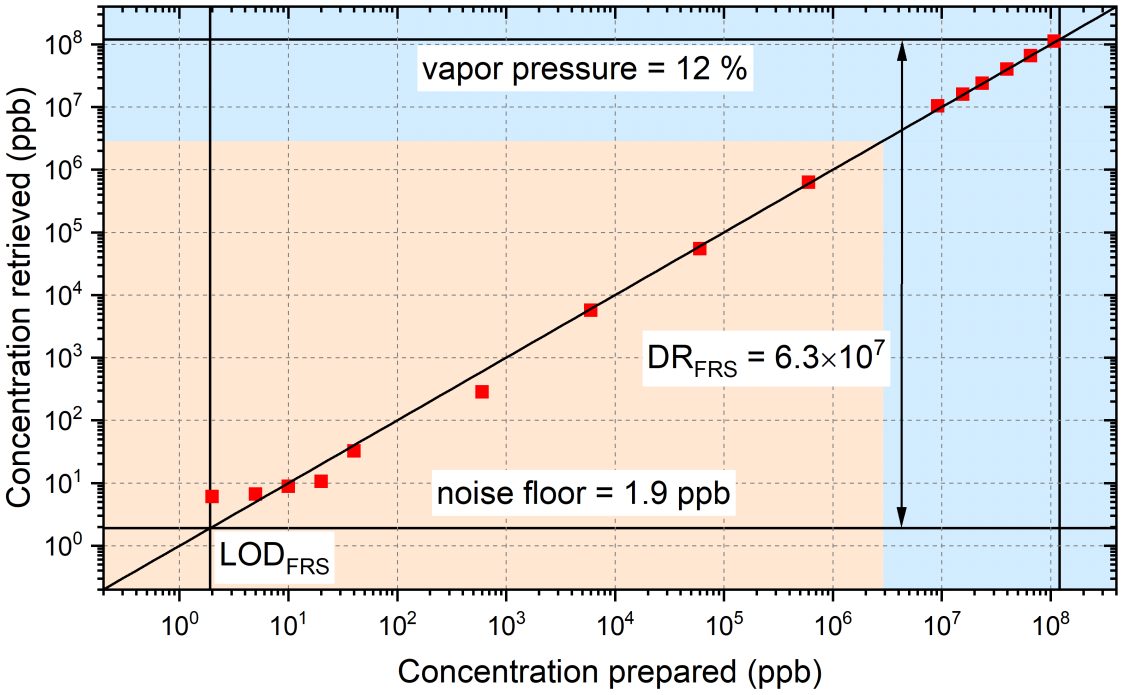

Figure 4.3: Dilution series for the FRS measurements. The retrieved concentrations are in good agreement with the prepared values and the LOD was determined to 1.9 ppb. The maximum concentration was 12 %, limited by the vapor pressure of methanol, which results in 6.3×10^7 retrievable concentration dynamic range using the CO-stretch mode of methanol. Effects from adsorption and contaminants together with bad SNR cause the deviations at low-ppb concentrations. The shaded areas indicate whether the concentration is retrieved in the time (orange) or frequency domain (blue), respectively.

The comparison of two reference traces was used for the calculation of the LOD of FRS. Each of these reference traces is the average of five individual scans. The two curves are then subtracted in the time domain, and a time window is applied to identify the background-free parts of the measurement.

The Fourier-transform of this time-filtered signal is calculated and the mean value (27-35 THz) determines the baseline value. Afterwards, a simulation was performed using one reference to compute the sample signal strength at 31 THz equal to this

baseline value. The concentration giving equal signal strength is then defined as the LOD and corresponds to a noise-equivalent concentration.
The obtained detection limit of 1.9 ppb, using a 45-cm long sample cell, competes well against the FTIR spectrometer and other instruments reported in the literature [35]. The retrievable concentration dynamic range using the two limits calculates to 6.3×10^7 and reflects the high intensity dynamic range of our laser system and the possibility to benefit from the time-domain nature of FRS.
In order to have a comparable limit of detection, we have to reference the LOD by the measurement time. The time-domain traces measured with EOS extend over a delay-range of 11 ps. Together with the scan velocity of the delay stage of $v_{\mathrm{delay}} = 0.4\,\mathrm{mm/s}$ and the speed of light, the laboratory time for a single trace is approximately 8.27 s. The effective measurement time is doubled to account for sample and reference scans. For the LOD in Figure 4.3, ten traces were used, which results in a total measurement time of 82.7 s. Taking the averaging time and sample cell length into account, FRS is two orders of magnitude more sensitive than the FTIR spectrometer. In comparison to state-of-the-art, spectrally narrowband gas-sensing [56], our laser source covers more than one octave (19.6-41.1 THz at the -30-dB-level). This enables investigation of complex molecular ensembles [31].
In the low-ppb regime, the data points deviate stronger from the expected values, because the molecular signal approaches the noise floor and the SNR decreases. Furthermore, adsorption and contaminants impact sample handling and prevent reliable preparation of ppt-level samples with the current vacuum system and protocol [41]. Therefore, new approaches to prepare ppt concentrations have to be considered. Besides ensuring cleanliness of the sample-handling with high vacuum, different concentrations can be prepared in a nitrogen-stream with heated components of the vacuum setup [43].

4.2.2 Gas-Phase Mixtures

The MIR spectrum obtained via IPDFG from our laser source covers the spectral range from 19.6 THz to 41.1 THz at the -30-dB-level. Usually, the spectral width is given at the FWHM [57]. However, due to the high dynamic range demonstrated in the previous section, the spectral intensity at the -30-dB-level is still sufficient for spectroscopic applications. In this section, we quantify the performance of our broadband

laser source in combination with FRS by analyzing sample mixtures with varying concentration ratios.

Figure 4.4 shows the measured and simulated spectrum of a test sample consisting of acetylene, methanol and methane together with the spectrum of the exciting laser field. The simulation is performed with the total complex absorption coefficient calculated as $\tilde{\alpha}_{\text{tot}} = \tilde{\alpha}_{\text{acetylene}} + \tilde{\alpha}_{\text{methanol}} + \tilde{\alpha}_{\text{methane}}$ and a time-delay window for Fourier transformation from 3 ps to 10 ps. The simulated coefficients in the plot correspond to 4 ppm acetylene, 0.84 ppm methanol and 75 ppm methane, and show excellent agreement with the measurement for methanol and acetylene. The slight deviations at the methane lines might be caused by the background already encountered in the time-domain trace.

The visible spectral features of acetylene and methane at the boundaries of our spec-

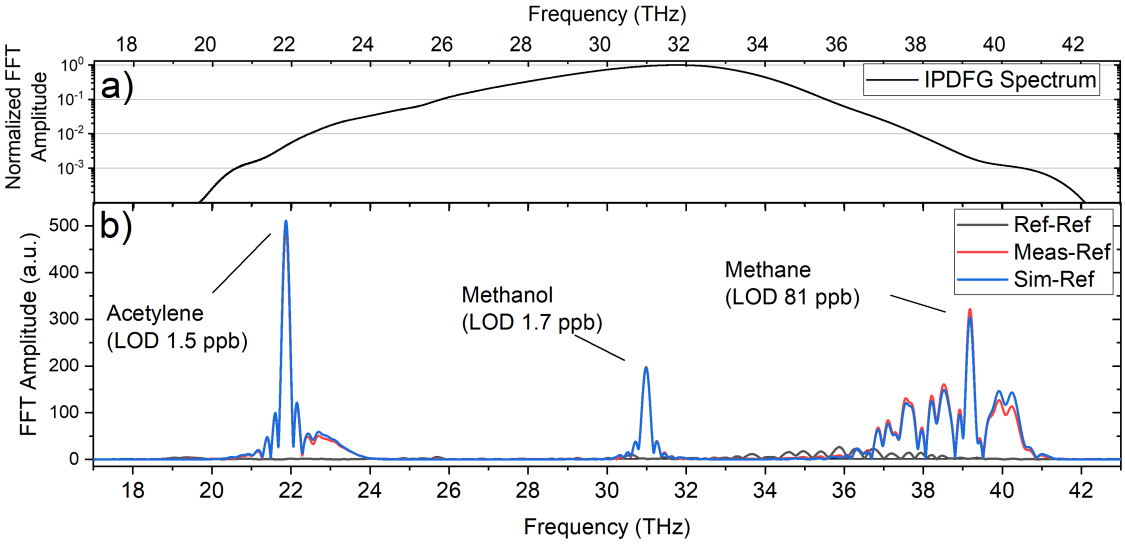

Figure 4.4: a) Spectral bandwidth of the instrument, corresponding to the MIR excitation spectrum generated via IPDFG. b) Fourier-transform of the time-filtered signal for a sample mixture consisting of acetylene, methanol and methane. The measurement agrees well with the simulated spectrum with 4 ppm acetylene, 0.84 ppm methanol and 75 ppm methane. The noise equivalent concentration detection limits were determined using the HITRAN line data.

trum reflect the broad coverage of our laser system. Smaller spectral intensity means that less sample molecules are excited causing a decreased amplitude of coherent

sample emission. This increases the LOD for acetylene and methane. Considering the different interaction cross section of each molecule, we determine the LOD for acetylene, methanol and methane in a mixture using the HITRAN line data with the total absorption coefficient stated above. For an averaging time of 490 s and the 45-cm long gas cell, we determine the limits to 1.5 ppb (acetylene), 1.7 ppb (methanol) and 81 ppb (methane). Although the averaging time has been increased by approximately a factor of six compared to the previous experiments, the LOD of methanol has not been improved by a factor $\sqrt{6}$. This will be investigated in the next section.
The limits obtained for acetylene and methane can compete with results from literature [35]. This demonstrates high sensitivity at the boundaries of the spectrum and highlights the unprecedented combination of sensitivity and specificity of our setup.

4.2.3 Towards ppt-Level Sensitivity

As we have seen before, ppb-level-sensitivity of the FTIR spectrometer already benefits biomedical applications (see Chapter 4.1). However, going towards the ppt range promises even deeper insights in samples with low-abundant biomolecules.
In order to exploit the full potential of our setup, we investigated the detection limit while increasing the averaging time to reach smaller detection limits. As the EOS scan velocity of each trace is optimized, this was done by averaging consecutively recorded reference traces and investigating the resulting LOD. Figure 4.5 shows the evolution of the LOD for methanol for three different measurements. The first two scans show a decreasing LOD up to the maximum averaging time of 331 s. The minimum LOD is determined to 913 ppt.
For the third scan the LOD decreases up to an averaging time of approximately 300 s. For higher averaging times, drifts in the experimental setup cause an increase in the LOD [58]. These effects most probably originate from drifts of the balancing in the EOS detection setup, which increases the detection noise floor on a time scale of minutes. Beam pointing drifts and changes in the gate pulse spectrum are two possible reasons for degrading the balancing performance. The averaging of multiple traces is affected by these drifts due to the slow scan with a mechanical delay stage. Future fast-scanning techniques promise solutions to tackle these problems [24][25]. This shows that ppt-sensitivities are already feasible with our setup. However, the onset of drifts is not reproducible, which is why further improvements of the setup sta-

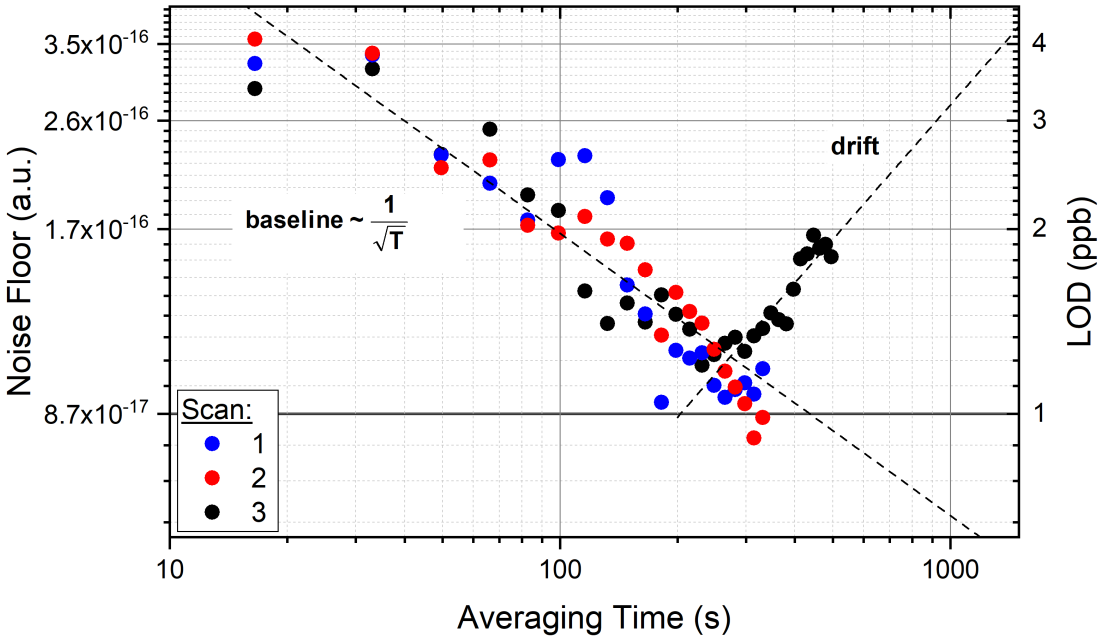

Figure 4.5: Noise floor and LOD as a function of the averaging time. The noise decreases up to approximately 300 s. Further averaging leads to increasing detection limits due to drifts in the detection setup. We determined a minimum LOD of 913 ppt for an average time of 314 s. The dashed lines indicate a linear fit for the two regimes mentioned in the plot.

bility are necessary.

In addition, scanning the gate-pulse delay only over the time window of interest would reduce the measurement time at a constant number of acquired traces, which also enables further averaging as the onset of drifts depends on the elapsed laboratory time. For the analysis of small concentrations we used the time window from 8 ps to 10 ps after the main pulse, which would enable a reduction of the laboratory time of the measurement by approximately a factor of five. Following the square-root line in Figure 4.5, this promises higher sensitivity with reproducible detection limits below 1 ppb. Experiments in the near future aim to verify these expectations experimentally. Potentially different time windows can be used, which might yield further improvements.

4.2.4 Sliding-Window Analysis

So far, we have only analyzed the time-domain signal of methanol between 8 ps and 10 ps after the excitation pulse, where the molecular signal of methanol only shows the strong Q-branch at 31 THz (see Figure 4.2) and not the rotational-vibrational spectrum expected from the simulation (see Figure 2.1). In the following, the time-domain evolution of the methanol signal is investigated with a sliding time-window analysis to obtain temporally and spectrally-resolved information about the molecular signal.
The time-domain trace for a simulated 60 ppm methanol sample is scanned by a 2-ps long time window to analyze the signal evolution as shown in Figure 4.6 a) for three time window positions. The starting point of the time window was varied from 2 ps to 50 ps. The Fourier transform of the time-filtered trace was computed and the peak value of the spectrum between 29 THz and 33 THz was determined. Figure 4.6 b) shows the normalized peak values plotted against the position of the time window. Up to 13 ps, the signal decreases exponentially as expected for the free induction decay of a single Lorentzian line.
At approximately 16.5 ps and 22.6 ps after the excitation pulse, the signal reveals characteristic peaks. This can be explained by the beating of several rotational modes [59]. At time zero of the few-cycle excitation, the emitted waves of the molecular oscillations are all in phase and therefore interfere constructively. From the beating signal of two superposed waves with frequency difference Δf we know that two frequencies show constructive interference again after a period [60]:

$$t_{\text{beating}} = \frac{1}{\Delta f} \tag{4.1}$$

The beating periods of 16.5 ps and 22.6 ps correspond to frequency differences of 2 cm^{-1} and 1.5 cm^{-1}, respectively. This correlates with the difference of the rotational lines in the P and R-branch of methanol. Therefore, the peak at 16.5 ps can be explained by constructive interference of the rotational lines of the P-branch and analogously for the R-branch at 22.6 ps. The two peaks occur separately due to the different spacing between the rotational lines of the two branches (details in Chapter 2). This interpretation is verified by the time-filtered spectra (see Figure 4.6 c)). Either the P- or the R-branch is dominant in the spectrum for the two delays. In the time window between 2 ps and 27 ps, all features of the rotational-vibrational spectrum expected from the simulation are reproduced.

The two strong peaks at 35 ps and 46 ps correspond to the second echo of the previously described beating signal. The signal at 35 ps reveals a step-like build-up, i.e., the constructive interference of the rotational lines of the P-branch is distributed over a longer time scale. This indicates that the frequency differences of the rotational lines within the P-branch are not exactly equal, which leads to different beating periods and therefore no single beating peak.

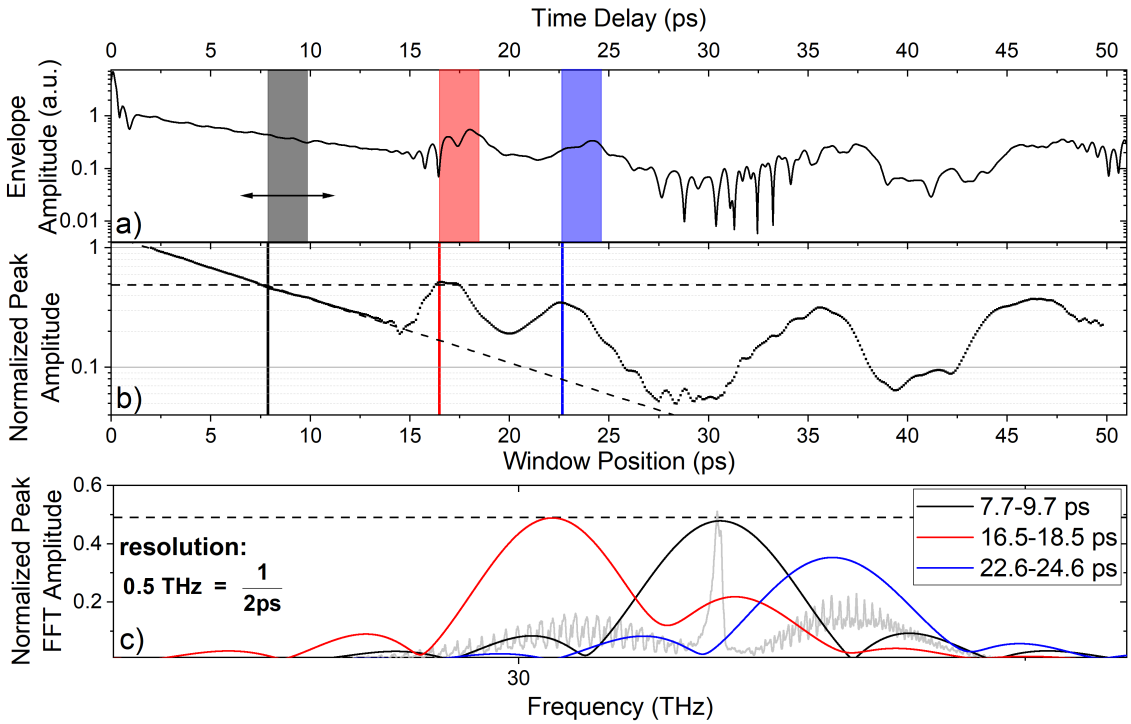

Figure 4.6: Sliding time-window analysis. a) Time-domain trace of 60 ppm methanol after impulsive excitation. b) Normalized peak amplitude of the time-filtered trace for varying time-window positions. The first 13 ps show an exponential decay of the amplitude. The peaks at 16.5 ps and 35 ps correspond to constructive interference of the rotational lines within the P-branch. Analogously, the peaks at 22.6 ps and 46 ps result from the R-branch lines. c) Fourier-transform of time-domain signal for different time-window positions. The methanol branches (see simulated spectrum in gray) are dominant at specific time delays. The time-window duration defines the resolution of the spectrum.

In principle, the time-domain evolution of the molecular signal can be used to measure low concentration ensemble components even with a strong molecular background signal. By choosing an appropriate time window, where the sample has a strong echo and the background has minimum signal, the signal-to-background ratio can be optimized. However, the position of the beating signal is specific for each molecule [59]. If the background has a strong echo at the same time position as the sample, the benefit of this time-domain analysis is reduced.
The evolution of the molecular signal is also helpful for understanding the spectra obtained with the enhancement cavity, presented in Chapter 4.3.
In general, it will depend on the investigated sample and the application whether time windows with strong beating signal benefit the sensitivity and specificity. Future experiments will investigate in more detail possible improvements of this time-modulation spectroscopy approach.

To conclude, we have demonstrated highly-sensitive gas-phase spectroscopy employing EOS over a broad spectral region (19.6-41.1 THz at the -30-dB-level). The results verify the unprecedented combination of detectable concentration range of more than seven orders of magnitude and an octave-spanning spectrum. For gas-phase spectroscopy of methanol and normalized with respect to measurement time and sample cell length, FRS is two orders of magnitude more sensitive than the FTIR spectrometer. The detection limits for a sample mixture consisting of acetylene (at 22 THz), methanol (at 31 THz) and methane (at 39 THz) are determined to be 1.5 ppb, 1.9 ppb and 81 ppb, respectively. This demonstrates high sensitivity over a broad spectral region.
Increasing the averaging time to reach ppt-level sensitivity was achieved, but further improvements of the setup stability are necessary in order to reproducibly reach even smaller detection limits. The analysis of the molecular time evolution revealed that the three branches of methanol are dominant at different time delays after the few-cycle excitation. Potential improvements in terms of sensitivity and specificity by choosing different time windows seem feasible.

4.3 Enhancement Cavity

In Chapter 3, we have introduced the concept of reflective input coupling in the framework of a bowtie cavity configuration. It enables broadband enhancement of MIR light. We will now proceed with experimental results using this setup to quantify the enhancement for gas-phase samples.
First, the time-resolved field recorded after reflection from the cavity is investigated employing EOS. The destructive interference towards the outside of the cavity can be examined for an “on resonance“ configuration as well as for a blocked cavity. Then, the background-free part, i.e., after the excitation pulse merges with the noise floor, of the transmitted and reflected time-domain traces is used to compute the spectra of the molecular signal. The resulting frequency-resolved information is used to quantify the spectral enhancement, with a gas-phase methanol test sample.
We employ the experimental setup shown in Figure 3.6 with a repetition rate of the Er:fiber laser oscillator of approximately 100 MHz. The oscillator output is reduced to 50 MHz using a pulse picker based on an electro-optic modulator, before being sent to the amplifier stages (see Chapter 3.3). We measure the repetition rate to $f_{\mathrm{rep}} = 50.001 MHz$. To obtain coherent superposition of subsequent pulses, the cavity length L_{c} is adjusted to:

$$L_{\mathrm{c}} = \frac{c}{f_{\mathrm{rep}}} \approx 5.996 m \tag{4.2}$$

Here, c denotes the speed of light in vacuum. Then, the cavity resonances may be observed on the oscilloscope by resolving the transmitted beam on a photodetector and the cavity length for locking can be chosen. As described in Chapter 3, the reflected NIR beam from the cavity is used for locking the oscillator repetition rate to the cavity.[2]

4.3.1 Time-Domain Analysis

As described in Chapter 3, we can shift the MIR and NIR resonances on the oscilloscope against each other using the CEO frequency f_{ceo}. In the following, the configuration with both resonances at the same position will be called “on resonance“. If the MIR resonance is not at the position of the NIR one used for locking, the signal will be referred to as “off resonance“. While the oscillator repetition rate is locked

[2]The experimental work was performed together with P. Sulzer, A. K. Raab and D. Gerz

to the cavity length, the reflected MIR pulse is sent to the EOS detection setup for field-resolved measurements.[3] After measuring the pulse for the “on resonance“ configuration, a beam dump was placed in front of a cavity mirror and the measurement was repeated. Both scans were conducted with 500 ppb of methanol inside the cavity chamber.
Figure 4.7 a) depicts the traces for the two configurations. The blocked cavity trace results from the light transmitted through the diamond input coupler. The “on resonance“ trace shows the interference between the seed pulse and the outcoupled intra-cavity pulse. Figure 4.7 b) and c) present the traces at the specified time positions after a band-pass filter (28-34 THz FWHM, Hann window) was applied. The signal amplitude of the main pulse is reduced in the resonant configuration compared to the blocked configuration. This visualizes the destructive interference at the output of the cavity if the locking mechanism works properly. The molecular signal of carbon dioxide, water vapor and methanol is enhanced (see delay 2.5-6 ps).
This demonstrates the path-length enhancement of the cavity in the time domain. By enhancing the molecular response, weak signals below the single-pass LOD can be detected.

4.3.2 Frequency-Domain Analysis

The background-free “tail“ of the time-domain traces is used to calculate the spectra of the molecular response via Fourier transformation. We consider the time-filtered electro-optic signal recorded after transmission and reflection from the cavity. These traces were recorded with a methanol test sample (500 ppb concentration) inside the cavity chamber in an air environment specifically tailored to achieve the optimum offset frequency (see Section 3.4).

Enhancement Cavity Transmission

Figure 4.8 depicts the spectra of the time-filtered (7.2-18.8 ps at FWHM, super-Gaussian of 3rd order), electro-optic signal recorded after transmission through the cavity together with their average. The “off resonance“ spectrum corresponds to a locking setting, where the carrier-envelope offset frequency f_{ceo} of the oscillator was chosen

[3] The measurements were performed together with P. Sulzer

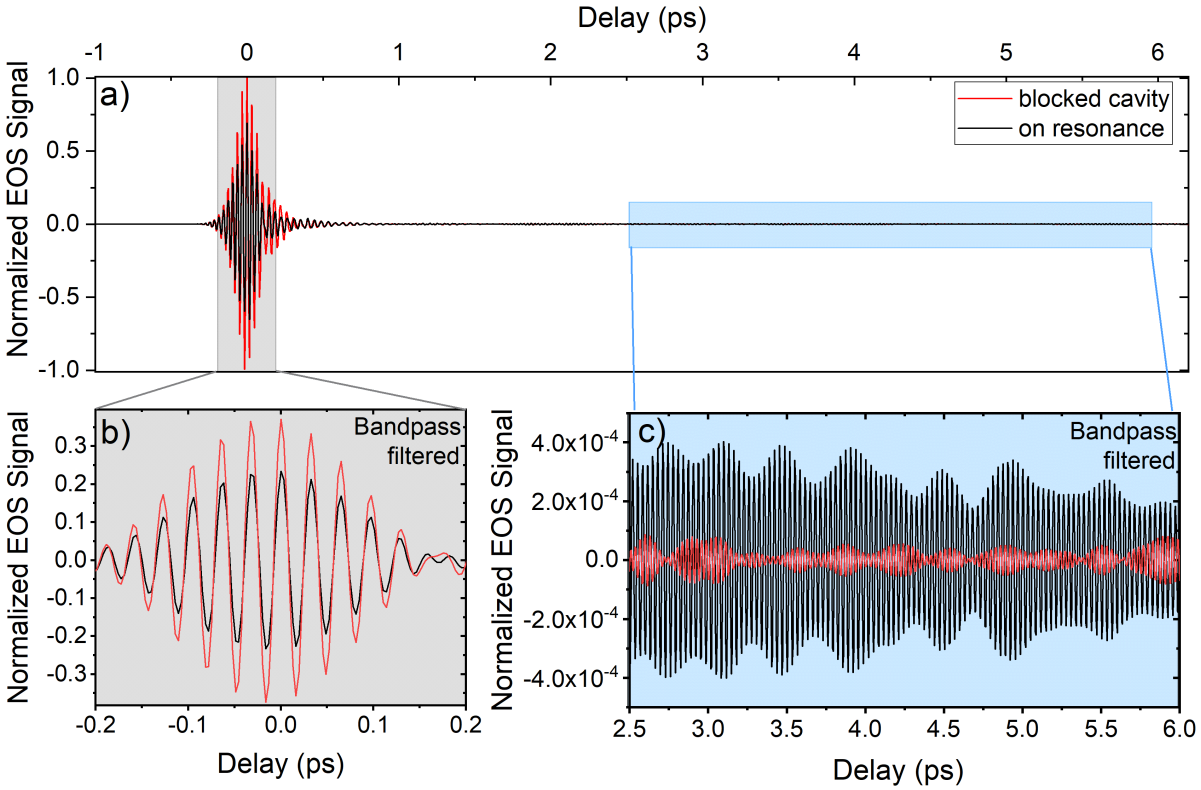

Figure 4.7: a) Electro-optic signal recorded after reflection from the cavity. The time-domain traces within the specified time window b) and c) are obtained after a band-pass filter (28-34 THz FWHM, Hann window) was applied.
b) Excitation pulse of the reflected cavity beam. The “on resonance“ pulse has a smaller amplitude because the seed pulse and the intra-cavity pulse destructively interfere at the output of the cavity. c) Background-free part of the trace revealing the molecular signal of methanol. The amplitude is enhanced for “on resonance“ configuration.

such that the MIR resonance does not overlap with the NIR resonance used for locking. This results in a spectral filtering of the MIR field preventing enhancement in the cavity (details see Chapter 3). The molecular lines for the “on resonance“ case are stronger than for the “off resonance“ configuration.

From the FTIR spectrometer diagnostic measurements we expect maximum enhancement at 31 THz. In order to quantify the peak enhancement using the molecular signal of methanol, we compare the “on resonance“ and the “off resonance“ spectral amplitude at 31 THz. However, for the given cavity parameters the methanol peak is not distinguishable in the “off resonance“ spectra of the transmitted cavity signal. There-

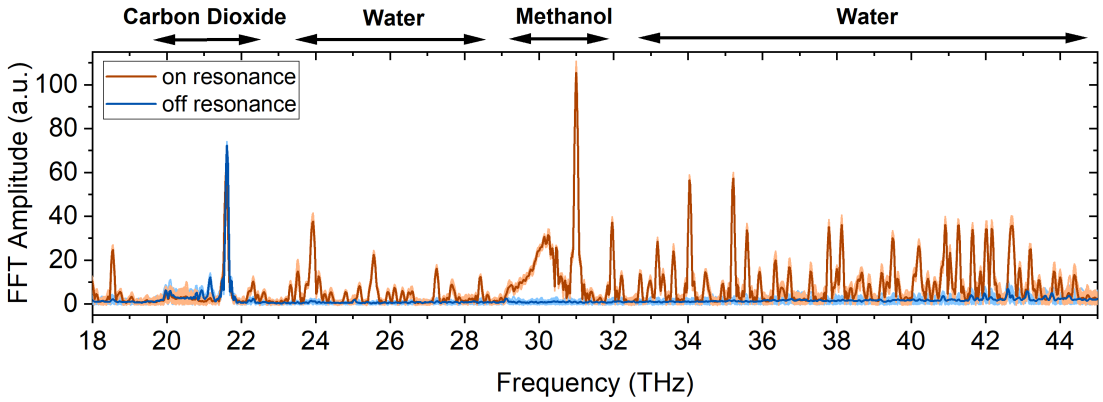

Figure 4.8: Fourier-transform of the time-filtered electro-optic signal recorded after transmission through the cavity. The main spectral features arise from carbon dioxide, methanol and water vapor. The “on resonance“ spectra show molecular lines from 18 THz to 45 THz highlighting the broad spectral coverage of our cavity setup.

fore, we cannot determine an experimental value for the peak enhancement using the transmitted curve. The ratio between the traces recorded after transmission through the cavity is proportional to the square of the input coupler transmission, which will be described in detail in future publications. With a given input coupler reflectivity of 4.3 %, we expect the “off resonance“ amplitude to be approximately two orders of magnitude smaller than the “on resonance“ amplitude. Nevertheless, the “on resonance“ spectrum in transmission illustrates the broad spectral coverage by more than one octave of our cavity setup. This proves that the cavity design is well-suited for broadband applications, but leaves the question about a quantitative value for the peak enhancement open.

Enhancement Cavity Reflection

Figure 4.9 visualizes the spectra of the time-filtered traces (5.0-20.5 ps at FWHM, super-Gaussian of 3rd order) recorded after reflection from the cavity. To estimate the limits of the cavity enhancement, we calculate the amplitude ratio AR between “on resonance“ and “off resonance“ configuration for molecular lines in the spectrum. However, only absorption lines with a SNR of at least three were used to prevent high enhancement factors by weak absorption lines. For the SNR, the FFT amplitude of the

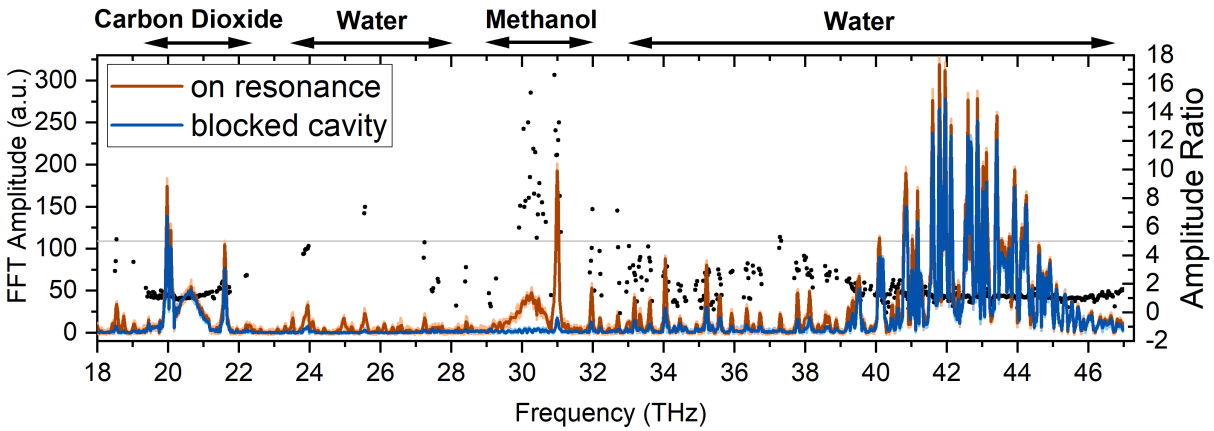

Figure 4.9: Fourier-transform of the time-filtered electro-optic signal recorded after reflection from the cavity (left axis). The main spectral features arise from carbon dioxide, methanol and water vapor. The absorption line amplitude ratio between “on resonance“ and blocked cavity is maximum around 31 THz and drops at the boundaries (black dots, right axis). The methanol signal can be distinguished in the spectra for the blocked cavity trace.

absorption line was divided by the baseline value. As baseline value, we calculated the root-mean-square value between 24 THz and 30 THz of the difference between two “off resonance“ spectra.

The spectral lines of carbon dioxide, methanol and water vapor are stronger for the “on resonance“ case. At the boundaries of the spectrum, the carbon dioxide as well as the water vapor lines have comparable amplitude for the “on resonance“ and the blocked cavity. The amplitude of both configurations is on the same order of magnitude because the “off resonance“ amplitude is not suppressed by the percent-level input coupler reflectivity as compared to the electro-optic signal recorded after transmission through the cavity. From the FTIR spectrometer diagnostic, we can locate the maximum enhancement of our setup at approximately 31 THz. This is confirmed by the spectral components between 30 THz and 31.5 THz because they reveal an absorption line amplitude ratio of up to 16. This enables the determination of the path-length enhancement in this configuration.

Figure 4.10 shows the spectral region of the CO-stretch mode of methanol of the electro-optic signal recorded after reflection from the cavity. The amplitude ratio at 31 THz is determined to 11.04. This value results from the strong Q-branch absorption line with better SNR compared to the other spectral components between 30 THz

and 31.5 THz and therefore provides a more reliable value for the AR.

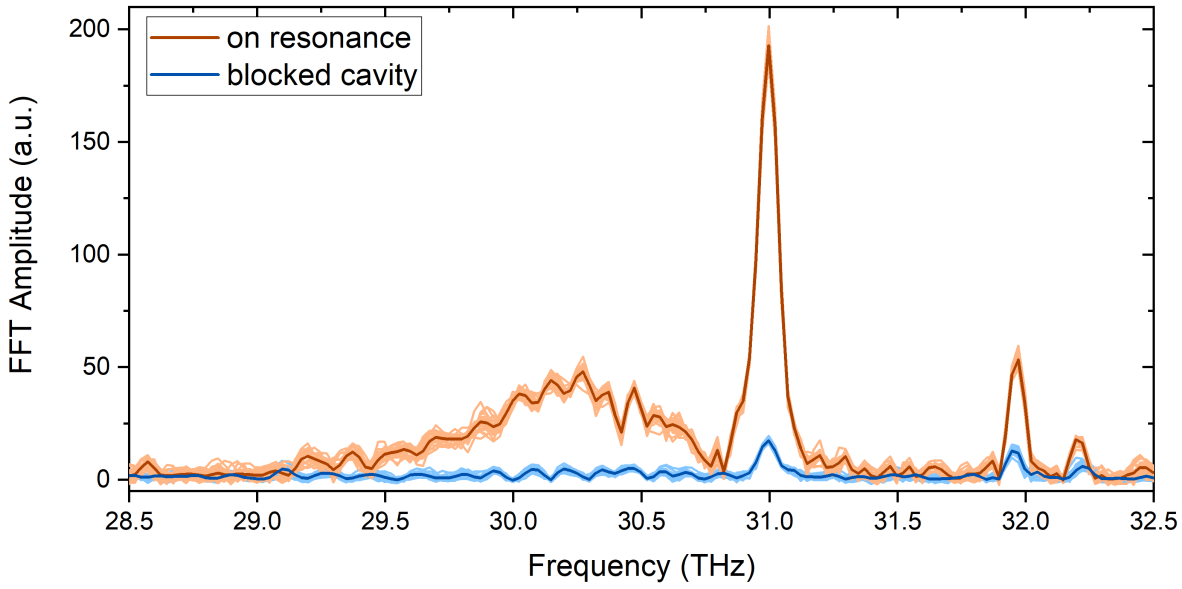

Figure 4.10: Fourier-transform of the time-filtered electro-optic signal recorded after reflection by the cavity. The molecular signal of methanol is enhanced by more than one order of magnitude for “on resonance“ configuration. If the cavity is blocked, the molecular signal arises from the interaction path before and after the cavity. In that case, the methanol peak at 31 THz is just above the noise floor.

We used a time window (5.0-20.5 ps) to filter the background-free part of the reflected cavity traces. This explains the missing R-branch at 31.6 THz (see Figure 2.1) due to the time evolution of the methanol signal, investigated in Section 4.2.4. The window duration was limited by multiple reflections at the DFG crystal. For the electro-optic signal recorded after reflection from the cavity, the amplitude ratio is equal to the ratio between the total path lengths for the two configurations. Using Equation 2.13, the AR can be written as:

$$AR = \frac{L_{\mathrm{tot}}^{\mathrm{on}}}{L_{\mathrm{tot}}^{\mathrm{off}}} = \frac{L_0 + PEF \cdot L_{\mathrm{c}}}{L_0} \tag{4.3}$$

With the “off resonance“ total path length $L_{\mathrm{tot}}^{\mathrm{off}}$ and the “on resonance“ total path length $L_{\mathrm{tot}}^{\mathrm{on}}$. Using the experimental values for the cavity length $L_{\mathrm{c}} = 5.996\,\mathrm{m}$ and the interac-

tion length outside the cavity $L_0 = 6.55\,\mathrm{m}$, we calculate the path-length enhancement PEF of the cavity to:

$$PEF = \frac{L_0 \cdot (AR - 1)}{L_c} = \frac{6.55\,\mathrm{m} \cdot (11.04 - 1)}{5.996\,m} \approx 10.9 \tag{4.4}$$

The effective path length is determined to $L_{\mathrm{eff}} = PEF \cdot L_c = 10.9 \cdot 5.996\,\mathrm{m} = 65.4\,\mathrm{m}$.
Using the baseline value from above and the peak amplitude at 31 THz, we estimate the LOD for the “on resonance“ case to 1.0 ppb for 80 s measurement time. This is comparable to the single-pass measurements in Chapter 4.2.1. In theory, we would expect an LOD of $\frac{0.45\,\mathrm{m}}{65.4\,\mathrm{m}} \cdot 1.9\,\mathrm{ppb} = 13\,\mathrm{ppt}$ from the path-length enhancement by the cavity.
The proof-of-principle cavity measurements were done with minimal optimization of the EOS setup. The resulting reduction in dynamic range of our MIR waveform in the frequency domain is on the order of 10^2 and explains the differences to the optimized single-pass experiments. The discrepancy in dynamic range may be explained by reflection losses of additional optics, imperfect spatial overlap of the gate and MIR pulse and modest balancing performance. An additional challenge is the contribution of water absorption and re-emission to the overall noise level, which will be addressed in future works.
Furthermore, for these cavity measurement no further noise optimization, e.g., Lock-in detection was implemented. The sampling rate for the EOS data acquisition is defined as the inverse integration time at each delay point of the mechanical delay stage. For the sampling rate in this measurement (approximately 2 kHz), we estimate the noise level to be a factor of ten higher than at a frequency of 10 kHz. Transmission through a chopping wheel reduces the MIR power by a factor of two, but can modulate our EOS signal for Lock-in detection. Combining both factors results in a factor of five improvement in the noise level compared to the measurement without Lock-in detection [13]. This gives us a theoretical detection limit of $\frac{1.0\,\mathrm{ppb}}{5} = 200\,\mathrm{ppt}$, which reveals the great potential for sensitive gas-phase spectroscopy.
To determine a bandwidth for the enhancement cavity, we used the absorption line amplitude ratio from Figure 4.9. For the absorption lines at 18.5 THz and 37.3 THz, the AR is still greater than five (see Figure 4.9) and therefore this spectral range will be defined as the bandwidth of our EC, spanning more than one octave. Note that not all lines within this bandwidth have an AR greater than five (see for example carbon

dioxide feature).

In conclusion, we measured the molecular signal recorded after reflection from the cavity. We observed destructive interference between the main seed pulse and the intra-cavity pulse, but at the same time an enhanced molecular signal. The cavity optics support the complete spectral range of our MIR light source. We quantified the peak path-length enhancement to 11.04 giving a power enhancement factor of 10.9. Together with the enhancement bandwidth (18.5-37.3 THz), the EC setup provides unique features for sensitive gas-phase spectroscopy.

5 Conclusion and Outlook

The goal of this thesis was a quantitative comparison between an FTIR spectrometry and FRS in the gas phase with a focus on the detectable concentration dynamic range and the sensitivity. In order to push the detection limit beyond the results obtained in single-pass with a 45-cm-long gas cell in the FRS instrument, a passive optical resonator was employed, increasing the effective interaction length.

In the present work, we benchmarked the performance of gas-phase samples of state-of-the-art time-integrating spectroscopy using an FTIR spectrometer. The LOD for the CO-stretch band of methanol at 31 THz [20] was determined to be 818 ppb (sample cell length: 14 cm; averaging time: 60 s) at a detectable concentration dynamic range of 6.1×10^4. The measurements were performed with 1 cm^{-1} resolution, which is sufficient to resolve all absorption bands with their rotational structure [31]. The retrieved and prepared concentrations from the dilution series are in good agreement, which validates the sample preparation protocols. Reliable sample concentrations are necessary for conclusions about the linearity of our spectroscopic methods.
FRS mitigates limitations seen for time-integrating MIR spectroscopy, e.g., modest noise figures and saturation problems of MIR detectors [4]. Employing EOS to achieve field-resolved detection we analyzed the coherently emitted field by molecules after excitation by a few-cycle infrared pulse to reach a new sensitivity regime combined with a broad spectral coverage for gas-phase samples. For methanol, we found a detection limit of 1.9 ppb (sample cell length: 45 cm; averaging time: 82.7 s), which is two orders of magnitude more sensitive than the FTIR spectrometer for similar parameters. We demonstrated a detectable concentration dynamic range of almost eight orders of magnitude reflecting the high intensity dynamic range of our instrument and the possibility to benefit from the time-domain nature of FRS.
Besides the high measurement dynamic range, we analyzed gas mixtures consisting

of acetylene, methanol and methane to illustrate spectroscopic detection of various low-abundant molecular species in the same measurement. We found a detection limit of 1.5 ppb (acetylene), 1.7 ppb (methanol) and 81 ppb (methane), which demonstrates the broad spectral coverage of our laser system (19.6-41.1 THz at the -30-dB-level).

By optimizing the averaging time of FRS, we achieved an LOD of 913 ppt for methanol, but the onset of drifts prevented further improvement by increasing the measurement time. Reducing the laboratory time by scanning a shorter time delay range shifts the onset of drifts to higher averaging times, thus enables gas-phase measurements at ppt-level sensitivity. The advantages of this approach depend on the chosen time window as different time delays show varying spectral amplitude of the molecular signal. Methanol reveals beating signals at 16.5 ps and 22.6 ps arising from constructive interference between the rotational lines within the P and R-branch. Choosing a time window at a beating peak of the sample might improve sensitivity and specificity. In conclusion, FRS has shown higher sensitivity and detectable concentration dynamic range than the FTIR spectrometer.

Further sensitivity improvements are realized by increasing the interaction length with the sample. By employing an EC in a bowtie configuration with highly reflective gold mirrors and internal, reflective input coupling using a diamond wedge, we achieved an effective interaction path length of 65.4 m. In our setup, this corresponds to a peak path-length enhancement factor of 10.9 of the Q-branch methanol signal at 31 THz. The maximum bandwidth of the setup supporting an amplitude ratio of five is determined to 18.5-37.3 THz, spanning more than one octave. The results were limited by the tradeoff between bandwidth and path-length enhancement [35]. High-sensitivity, broadband infrared spectroscopy is relevant for biomedical applications due to the diversity of low-abundant molecules in biological samples for potential health-state monitoring [5][10][55].

To conclude, in the scope of this master thesis an unprecedented combination of sensitivity and broad spectral coverage was demonstrated employing FRS for gas-phase samples. It was shown that ultra-broadband ECs have the potential to open further avenues for spectroscopic applications relying on high sensitivity of gas-phase samples.

Appendix

Data Archiving

The raw data of the experiments and the python scripts for the simulation as well as the data processing can be found on the data archive server of the Laboratory for Attosecond Physics at the Max-Planck-Institute of Quantum Optics:
//afs/ipp-garching.mpg.de/mpq/lap/publication-archive/theses/2021/Fürst, Lukas (MSc)

Injection Protocol

The following protocol describes the gas sample preparation using the Injection protocol from chapter 3.

Protocol: Quantitative Gas Measurements

Version: 1.2 12th of May 2021

Materials and Equipment:

- Gas sampling bulb including Septa (used only once) and two built-in valves (https://www.sigmaaldrich.com/catalog/product/supelco/22144u?lang=de&region=DE)
- Tubings, adapters and valves for connection of gas sampling bulb and syringes with the vacuum system
- Nitrogen bottle (with pressure reducing valve and connectors)
- Hamilton syringe for liquid handling (i.e. volume 50 µl with 1 µl division) (https://www.bgb-info.com/product.php?productid=61601&cat=34625&page=1)
- Gastight Hamilton syringe with valve for gas handling (i.e. volume 100 µl with 1 µl division) (https://www.bgb-info.com/product.php?productid=1006884&cat=34668&page=1)
- “Dosys all glass” syringe (250 ml) (https://www.socorex.com/en/laboratory/syringe-pipettes/dosys/all-glass-155-all-glass-syringes)
- Valves for 250 ml syringe (https://www.fishersci.de/shop/products/discofix-c-latex-free-three-way-valves/10199361#?keyword=b+braun+discofix)
- Septum for 250 ml syringe (https://www.bgb-info.com/product.php?productid=1006492)
- Gas bag (https://www.sigmaaldrich.com/catalog/product/supelco/24654?lang=de&region=DE)
- Gas cell with KBr/ZnSe windows, pressure monitoring devices, connector tubes and vacuum pumps

General Remarks:

- Keep a clean working environment (e.g. avoid dust).
- When working with low gas concentration, proper cleaning of the equipment is required beforehand to avoid any contaminants (see cleaning section).
- When doing a dilution study, one should start with the lowest concentrations, otherwise the high concentration from before might contaminate the low concentration measurements.
- When measuring different gas samples at very low concentrations (low ppb-range), one should use independent equipment for gas handling (e.g. one gas bulb/one 250 ml syringe for each specimen).

Preparation of Stock Gas Solution (≈30 min):

1. Purge tubes with pressurized air and nitrogen, then evacuate and flush with nitrogen (repeat once).
2. Assembly cleaned gas bulb (insert valves and septum).
3. Connect gas bulb to the vacuum system via tubings.
4. Open valves and evacuate gas sampling bulb (10^{-1} mbar range is enough for substances that evaporate quickly).
   NOTE: If the pressure is measured close to the pump, leakage can cause much higher pressure in the bulb. The connection to bulb might be small, so evacuation takes longer.
5. Close the valves.
6. For very low concentrations, wear gloves for the next step.
7. Use clean Hamilton syringe (for liquids) to take out a certain amount of the liquid sample without having air bubbles in the syringe. This can be achieved by pumping up and down relatively fast. At some point one should only have liquid without air in the syringe.
8. Fill the sample into the gas bulb via the septum. It should evaporate immediately. If not, the pressure was not low enough and one can heat up the gas bulb (e.g. temperatures above 65°C for methanol).
9. Fill the gas sampling bulb with nitrogen until atmospheric pressure is reached.
   a. Fill a gas bag with nitrogen. Make sure the tubings and the bag are free of contaminants. This can be achieved if the bag is only used for nitrogen and by evacuation and flushing with nitrogen.
   b. Open the valves to the gas sampling bulb. The nitrogen will flow into the bulb until atmospheric pressure is reached.
   c. Close the valves and disconnect the bag and the bulb.
10. The concentration in the stock solution can be calculated in a table:

	Stock solution: injected 40 µl liquid to 1000 ml (c = 2.2 %)				Stock solution: injected 150 µl liquid to 1000 ml (c = 8.3 %)			
Extracted gas [µl]	13	26	46	80	12	25	50	100
Concentration in 250 ml N2 [ppm]	0.4	0.8	1.4	2.5	4.0	8.3	16.6	33.2

Dilution of Stock Solution (≈5 min):

1. Fill clean gas syringe with 250 ml nitrogen.
    a. Connect syringe to system and open valves to evacuate.
    b. Purge the syringe twice by letting nitrogen flow in and then evacuate again.
    c. Fill syringe with 250 ml nitrogen and then close valve.
2. Take desired amount of stock gas from gas bulb with gas tight syringe.
    a. Go through the septum and open the valve.
    b. Pump a few times with the syringe and take out the desired volume of stock gas.
    c. Close the valve and remove the syringe.
3. Fill the sample into the 250 ml glass syringe.
    a. Go through the septum of the gas syringe.
    b. Open the valves and fill sample in by pumping a few times with the syringe.

Filling of the Measurement Cell (≈1 min):

1. Evacuate the gas cell and the vacuum system.
2. Close the valve towards the pump and flush with nitrogen. Then evacuate the vacuum system (repeat once).
3. Open the valves to the gas syringe filled with the sample and monitor the pressure.
4. Fill the gas cell until atmospheric pressure is reached and close the valves.
5. Sample preparation is finished.

Cleaning of the Equipment:

Vacuum system:

1. Use pressurized air and nitrogen to purge system for a couple of minutes. Make sure that the system is open that no high pressure can build up.
2. When working with low concentrations, longer purging might be required.
3. Heating the tubings (up to 60°C) improves the cleanness.
4. Evacuate the system and flush with nitrogen (repeat once).
   NOTE: Consider pressure working range of turbo pump!

Gas cell:

1. Disassemble the cell.
2. Make sure that the KBr windows are not cleaned with water or solvent!
3. Other parts can be cleaned with solvent (make sure the solvent gives an acceptable background in the spectrum and does not harm the epoxy glue).
4. Clean with distilled water afterwards.
5. Components can be left in oven over night. The glue can withstand up to 120°C but consider the shear strength in the specification sheet. Thin windows can break easily by the heated glue.

Gas sampling bulb:

1. Disassemble and throw away the septum.
2. Fill solvent into the gas bulb (make sure the solvent gives an acceptable background in the spectrum).
3. Shake the bulb and let solvent out. Repeat with deionized water.
4. The glass bulb can be put into the oven. The maximum temperature is not specified. The technical service determines the limit by the Teflon valves at a temperature of 260°C. Significantly lower temperatures are recommended.
5. Valves and PUN tubes (up to 60°C) can be put into the oven.

Small Hamilton syringes:

1. Clean syringes with solvent and deionized water (make sure the solvent gives an acceptable background in the spectrum).
2. Let syringes dry in a disassembled state. They can be put into the oven (up to 115°C).
3. Use the cleaning devices provided for the syringe.

Large (250 ml) Hamilton syringes:

1. Remove and throw away the valve.
2. Disassemble the syringe and clean with solvent and deionized water.
   NOTE: Do not assemble syringe if there is water inside the cylinder. Even small amounts can lead to blocking of the plunger.
3. The components can be put into oven (up to 160°C).
4. Carefully try to insert the plunger straight back into the cylinder.

List of Figures

Bibliography

[1] Matthew J Baker et al. “Using Fourier transform IR spectroscopy to analyze biological materials”. In: *Nature protocols* 9.8 (2014), p. 1771.

[2] Albert Schliesser, Nathalie Picqué, and Theodor W Hänsch. “Mid-infrared frequency combs”. In: *Nature photonics* 6.7 (2012), pp. 440–449.

[3] Marinus Huber. “Field-Resolved Infrared Spectroscopy”. PhD thesis. Ludwid-Maximilians-Universität, 2020.

[4] Ioachim Pupeza et al. “Field-resolved infrared spectroscopy of biological systems”. In: *Nature* 577.7788 (2020), pp. 52–59.

[5] Zanyar Movasaghi, Shazza Rehman, and Dr Ihtesham ur Rehman. “Fourier transform infrared (FTIR) spectroscopy of biological tissues”. In: *Applied Spectroscopy Reviews* 43.2 (2008), pp. 134–179.

[6] Henry Timmers et al. “Molecular fingerprinting with bright, broadband infrared frequency combs”. In: *Optica* 5.6 (2018), pp. 727–732.

[7] Jane Hodgkinson and Ralph P Tatam. “Optical gas sensing: a review”. In: *Measurement Science and Technology* 24.1 (2012), p. 012004.

[8] Kiran Sankar Maiti et al. “Sensitive spectroscopic breath analysis by water condensation”. In: *Journal of breath research* 12.4 (2018), p. 046003.

[9] Iwona Belczacka et al. “Proteomics biomarkers for solid tumors: Current status and future prospects”. In: *Mass spectrometry reviews* 38.1 (2019), pp. 49–78.

[10] Marinus Huber et al. “Stability of person-specific blood-based infrared molecular fingerprints opens up prospects for health monitoring”. In: *Nature communications* 12.1 (2021), pp. 1–10.

[11] Nathalie Picqué and Theodor W Hänsch. “Frequency comb spectroscopy”. In: *Nature Photonics* 13.3 (2019), pp. 146–157.

[12] Shibdas Banerjee and Shyamalava Mazumdar. “Electrospray ionization mass spectrometry: a technique to access the information beyond the molecular weight of the analyte”. In: *International journal of analytical chemistry* 2012 (2012).

[13] Christina Hofer. “Detection Efficiency and Bandwidth Optimized Electro-Optic Sampling of Mid-Infrared Waves”. PhD thesis. Ludwid-Maximilians-Universität, 2021.

[14] Qi Wu and X-C Zhang. “Free-space electro-optic sampling of terahertz beams”. In: *Applied Physics Letters* 67.24 (1995), pp. 3523–3525.

[15] Ian Coddington, William C Swann, and Nathan R Newbury. “Time-domain spectroscopy of molecular free-induction decay in the infrared”. In: *Optics letters* 35.9 (2010), pp. 1395–1397.

[16] Aleksandra Foltynowicz et al. “Quantum-noise-limited optical frequency comb spectroscopy”. In: *Physical review letters* 107.23 (2011), p. 233002.

[17] A Manninen et al. “Versatile multipass cell for laser spectroscopic trace gas analysis”. In: *Applied Physics B* 109.3 (2012), pp. 461–466.

[18] TP Butler et al. “Watt-scale 50-MHz source of single-cycle waveform-stable pulses in the molecular fingerprint region”. In: *Optics letters* 44.7 (2019), pp. 1730–1733.

[19] Hermann Haken and Hans C Wolf. *Molekülphysik und Quantenchemie: Einführung in die experimentellen und theoretischen Grundlagen*. Springer-Verlag, 2006.

[20] Virtual Planetary Laboratory - University of Washington. *Methanol (CH3OH)*. Apr. 2021. URL: `http://vpl.astro.washington.edu/spectra/HITRAN2008/molecule_pages/methanol.htm`.

[21] Peter R Griffiths. “Fourier transform infrared spectrometry”. In: *Science* 222.4621 (1983), pp. 297–302.

[22] Ron Williams. “Applications of Fourier transform spectrometry in the ultraviolet, visible, and near-IR”. In: *Applied Spectroscopy Reviews* 25.1 (1989), pp. 63–79.

[23] P Jaakkola et al. “Instrumental resolution considerations for Fourier transform infrared gas-phase spectroscopy”. In: *Applied spectroscopy* 51.8 (1997), pp. 1159–1169.

[24] B Süss, F Ringleb, and J Heberle. “New ultrarapid-scanning interferometer for FT-IR spectroscopy with microsecond time-resolution”. In: *Review of Scientific Instruments* 87.6 (2016), p. 063113.

[25] Nathan R Newbury, Ian Coddington, and William Swann. “Sensitivity of coherent dual-comb spectroscopy”. In: *Optics express* 18.8 (2010), pp. 7929–7945.

[26] Philip CD Hobbs. “Ultrasensitive laser measurements without tears”. In: *Applied optics* 36.4 (1997), pp. 903–920.

[27] Guilhem Gallot and D Grischkowsky. “Electro-optic detection of terahertz radiation”. In: *JOSA B* 16.8 (1999), pp. 1204–1212.

[28] Michael Porer, Jean-Michel Ménard, and Rupert Huber. “Shot noise reduced terahertz detection via spectrally postfiltered electro-optic sampling”. In: *Optics letters* 39.8 (2014), pp. 2435–2438.

[29] Philipp Sulzer et al. “Determination of the electric field and its Hilbert transform in femtosecond electro-optic sampling”. In: *Physical Review A* 101.3 (2020), p. 033821.

[30] W. Demtröder. *Laserspektroskopie 1: Grundlagen*. SpringerLink : Bücher. Springer Berlin Heidelberg, 2011. ISBN: 9783642213069.

[31] Zoltán Bacsik, János Mink, and Gábor Keresztury. “FTIR spectroscopy of the atmosphere. I. Principles and methods”. In: *Applied Spectroscopy Reviews* 39.3 (2004), pp. 295–363.

[32] Antonio Rogalski. *Infrared Detectors*. CRC Press, 2010.

[33] AA Lanin et al. “Time-domain spectroscopy in the mid-infrared”. In: *Scientific Reports* 4.1 (2014), pp. 1–8.

[34] R. Paschotta. *optical heterodyne detection*. URL: `https://www.rp-photonics.com/optical_heterodyne_detection.html` (visited on 05/06/2021).

[35] Ann-Kathrin Raab. “Ultra-Broadband Mid-Infrared Enhancement Cavities for Gas-Phase Spectroscopy”. An optional note. MA thesis. TU Munich, Oct. 2020.

[36] R Jason Jones and Jun Ye. “Femtosecond pulse amplification by coherent addition in a passive optical cavity”. In: *Optics letters* 27.20 (2002), pp. 1848–1850.

[37] Warren Nagourney. *Quantum electronics for atomic physics and telecommunication*. OUP Oxford, 2014.

[38] Simon Holzberger. “Enhancement cavities for attosecond physics”. PhD thesis. LMU München, 2015.

[39] Gianluca Gagliardi and Hans-Peter Loock. *Cavity-enhanced spectroscopy and sensing*. Vol. 179. Springer, 2014.

[40] H Frank Gibbard and Jefferson L Creek. “Vapor pressure of methanol from 288.15 to 337.65. deg. K”. In: *Journal of Chemical and Engineering Data* 19.4 (1974), pp. 308–310.

[41] Robert J Yokelson et al. “Evaluation of adsorption effects on measurements of ammonia, acetic acid, and methanol”. In: *Journal of Geophysical Research: Atmospheres* 108.D20 (2003).

[42] Irving Langmuir. “The adsorption of gases on plane surfaces of glass, mica and platinum.” In: *Journal of the American Chemical society* 40.9 (1918), pp. 1361–1403.

[43] Timothy J Johnson, Robert L Sams, and Steven W Sharpe. “The PNNL quantitative infrared database for gas-phase sensing: a spectral library for environmental, hazmat, and public safety standoff detection”. In: *Chemical and Biological Point Sensors for Homeland Defense*. Vol. 5269. International Society for Optics and Photonics. 2004, pp. 159–167.

[44] Ian Mills et al. *Quantities, units and symbols in physical chemistry/prepared for publication by Ian Mills...[et al.]* Oxford; Boston: Blackwell Science; Boca Raton, Fla.: CRC Press [distributor], 1993.

[45] Roman V Kochanov et al. “HITRAN Application Programming Interface (HAPI): A comprehensive approach to working with spectroscopic data”. In: *Journal of Quantitative Spectroscopy and Radiative Transfer* 177 (2016), pp. 15–30.

[46] Daniel Gerz et al. “Mid-infrared long-pass filter for high-power applications based on grating diffraction”. In: *Optics letters* 44.12 (2019), pp. 3014–3017.

[47] Christian Gaida et al. “High-power frequency comb at 2 μm wavelength emitted by a Tm-doped fiber laser system”. In: *Optics letters* 43.21 (2018), pp. 5178–5181.

[48] Ernst Fill et al. “A pellicle coupled optical resonator”. In: *The European Conference on Lasers and Electro-Optics*. Optical Society of America. 2019, cf_p_60.

[49] Justin Torgerson and Warren Nagourney. “Tunable cavity coupling scheme using a wedged plate”. In: *Optics communications* 161.4-6 (1999), pp. 264–266.

[50] Robert L Olmon et al. “Optical dielectric function of gold”. In: *Physical Review B* 86.23 (2012), p. 235147.

[51] HR Phillip and EA Taft. “Kramers-Kronig analysis of reflectance data for diamond”. In: *Physical Review* 136.5A (1964), A1445.

[52] TW Hansch and B Couillaud. “Laser frequency stabilization by polarization spectroscopy of a reflecting reference cavity”. In: *Optics communications* 35.3 (1980), pp. 441–444.

[53] Nicolai Lilienfein et al. “Enhancement cavities for few-cycle pulses”. In: *Optics letters* 42.2 (2017), pp. 271–274.

[54] Simon Holzberger et al. “Enhancement cavities for zero-offset-frequency pulse trains”. In: *Optics letters* 40.10 (2015), pp. 2165–2168.

[55] Philipp E Geyer et al. “Revisiting biomarker discovery by plasma proteomics”. In: *Molecular systems biology* 13.9 (2017), p. 942.

[56] Teemu Tomberg et al. “Sub-parts-per-trillion level sensitivity in trace gas detection by cantilever-enhanced photo-acoustic spectroscopy”. In: *Scientific reports* 8.1 (2018), pp. 1–7.

[57] R. Paschotta. *time-bandwidth product*. URL: `https://www.rp-photonics.com/time_bandwidth_product.html` (visited on 05/17/2021).

[58] PO Werle, R Mücke, and F Slemr. “The limits of signal averaging in atmospheric trace-gas monitoring by tunable diode-laser absorption spectroscopy (TDLAS)”. In: *Applied Physics B* 57.2 (1993), pp. 131–139.

[59] Rune Hylsberg Jacobsen, DM Mittleman, and MC Nuss. “Chemical recognition of gases and gas mixtures with terahertz waves”. In: *Optics Letters* 21.24 (1996), pp. 2011–2013.

[60] Dieter Meschede. *Gerthsen physik*. Springer-Verlag, 2015.

Acknowledgments

I would like to thank Ferenc Krausz and Ioachim Pupeza for the grand opportunity to work in the Attoworld team in the framework of my master's thesis. Thank you Ioachim for supporting me since my first day as a Bachelor student in 2019.
I would like to express my gratitude to Christina, Daniel, and Philipp. I learned so much from you while working together in the lab and thanks for the helpful feedback to my thesis.
Thanks also to Anka, Ernst and Maxi for sharing their experience with me and helping me if I had questions concerning cavities, programming, and a lot more.
Thanks to Kiran for helping me in the first days of my project and to Marinus and Frank for all their support.
Thanks to Vladimir, Daniel, and Bernd for sharing their FTIR spectrometer with me.
Thanks to Philip for enjoyable lunch breaks, the administrative and technical stuff, and all other helpful people at LMU in Garching.
Finally, words cannot describe how grateful I am for the constant support of my parents, Beate and Michael, and Elisabeth especially in difficult times.
Thank you all.

Eidesstattliche Erklärung

Hiermit erkläre ich, die vorliegende Arbeit selbstständig verfasst zu haben und keine anderen als die in der Arbeit angegebenen Quellen und Hilfsmittel benutzt zu haben.

Lukas Fürst Munich, June 16, 2021